A nonlocal kernel-based continuum damage model for compaction band formation in porous sedimentary rock

Enrique M. del Castillo¹, Jun Geng¹, and Ronaldo I. Borja^{1*}.

Summary. We propose a novel continuum damage model for describing the propagation of compaction bands formed by grain crushing in porous sedimentary rock using the kernel-based approximation and discretization of the meshfree Lagrangian smoothed particle hydrodynamics (SPH) method. In the model, damage is assumed to be caused by grain crushing, and the effects of plasticity are incorporated through a critical state type model which depends on a degradation function designed to capture the abrupt onset of pore collapse following grain crushing. In doing so, we account for the two main forces understood to drive compaction band formation, brittle failure at the grain scale, and plastic dissipation. Through the smoothing length parameter, the SPH method possesses nonlocal properties intrinsic to the method, allowing for the development of a nonlocal integral form of the equivalent strain variable used to compute the damage in addition to a distinct gradient enhanced approach that when discretized using SPH is endowed with two characteristic length scales. We compare and contrast both formulations, as well as the roles of the different length scales. We evaluate our model by performing numerical experiments on Bentheim and Berea sandstone as well as on Tuffeau de Maastricht, in both notched and unnotched specimens, matching experimentally observed results such as a transition from high-angled bands to horizontal bands with increasing confining pressure, and similar compaction band styles to those visible in the field. We lastly consider the effects of material heterogeneity on samples of Tuffeau de Maastricht noting that our model produces precursory low-magnitude localization events which may develop into persistent compaction bands involving localized grain crushing, which is consistent with our understanding of compaction band formation.

Keywords. Compaction bands; Continuum Damage Model; Smoothed Particle Hydrodynamics; Porous Sandstone; Grain Crushing

1 Introduction

Deformation bands are narrow tabular zones of localized deformation observed in soil, rocks, and other geologic materials. Stress concentrations produced by geometric considerations such as holes, voids, or notches, or abrupt variations in material strength or density can all lead to the development of deformation bands. Borja and Aydin [15] and Aydin et al. [7] developed a framework based on geologic principles and bifurcation theory to interpret and classify different deformation band types arising in numerical simulations of geologic materials. Specifically, the value of the dot product between a unit eigenvector of the acoustic tensor and the normal vector representing the critical band orientation was used to distinguish the different band types, a result that ultimately depends on the type of constitutive model used in the simulation. Various other approaches based on the dominant deformation mode within the band, the type of loading condition, or the orientation of the resulting band relative to the principal stress direction have been proposed to group together the vast array of existing deformation bands observed both in the field and in experimental testing of geologic materials [48] [98]. In highly porous sedimentary rocks, a type of deformation band known as a compaction band typically forms perpendicular to the direction of maximum principal stress and consists of compressive deformation with little to no shear offset. Compaction bands have also been observed to develop in other granular and porous materials such as snow [8], foams [9], honeycomb structures [78], and pharmaceutical powders [106].

¹Department of Civil and Environmental Engineering, Stanford University, Stanford, CA 94305, USA,

^{*}Corresponding author, e-mail: borja@stanford.edu

Since being first identified in situ in the Navajo Sandstone of Utah by the work of Mollema and Antonellini [69], compaction bands have been studied extensively in laboratory and field investigations. Based on field studies, compaction bands are generally subdivided into pure compaction bands and shear-enhanced compaction bands, where the latter propagate obliquely (38° to 53°) relative to the maximum principal stress direction [41]. In the Valley of Fire in southeastern Nevada, Eichhubl et al. found that in the Aztec sandstone, shear-enhanced compaction bands formed either individually or as wiggly bands consisting of linked shear-enhanced compaction band segments [41]. A considerable amount of variability in the angles between the shear-enhanced compaction band segments and in the degree of sharpness of the hinges led Liu et al. to coin the terms chevron band for sharp 90° joined segments and wavy bands for the smoother more undulated types [61]. Observations from compaction bands both in the field and in laboratory setting demonstrate that compaction bands are accompanied by a marked decrease in porosity and permeability between the compaction band and the surrounding host rock. This permeability reduction can have profound effects on the flow and extraction performance of geological reservoirs for purposes of hydrocarbon production, CO₂ storage, and hazardous waste disposal [50, [77], [89], motivating efforts to develop computational methodologies for forward-modeling of compaction band formation and propagation.

Compaction bands in both pure and shear-enhanced forms have been experimentally observed to occur in stress states native to the transitional regime between brittle faulting and cataclastic flow [105]. At high confining pressure cataclastic flow dominates in porous rock, leading to grain crushing, reduced porosity, grain rearrangement, and ultimately material hardening. Under low confining pressure, brittle faulting or shear localization take precedence over cataclastic flow and are generally associated with cracking between the grains through the intergranular bonds or matrix at the microscale (grain scale), inducing slip, grain rotation, dilatancy, and strain softening [68, 105]. At the macroscale (continuum-scale), shear localization and brittle faulting generally form at the orientations provided by Coulomb at $45^{\circ} \pm \varphi/2$ with respect to the maximum principal stress direction, where φ is the friction angle, whereas, zones of grain crushing localize into homogeneously distributed so-called high-angle bands or compaction bands.

Despite the grain-scale origin for the physics governing compaction band formation, numerical simulations operating at the grain scale such as using the discrete element method (DEM) 40,66 have encountered many challenges including issues relating to computational cost and scalability past the grain scale, an inability to reproduce deformation patterns observed in the field, and susceptibility to constitutive assumptions at the grain scale which may not translate to the continuum scale. Continuum approaches have been the preferred avenue for numerical or theoretical analysis of compaction bands. Continuum-based mechanistic characterizations of compaction bands must cope with both the aforementioned grain crushing and grain-scale brittle deformation in addition to plastic dissipation, as these two overarching dissipation mechanisms control the emergence of compaction bands 102. To date, most previous research has only incorporated the effects of plastic deformation 16, 25, 29, 59 which generally permits the computational simulation of incipient compaction band formation, but may prove insufficient for thoroughly modeling the longer-term evolution of these localization modes. Nevertheless, valuable insight has been gained. For example, Issen and Rudnicki demonstrated that compaction band propagation could be captured in porous materials by using a yield surface with a cap using bifurcation analysis 54. The numerical simulations of Liu et al., employed a cap model and also mirrored this finding, concluding that the shape of the compaction bands shape depended on the aspect ratio of the yield surface ellipse, in turn a function of porosity 62.

From a computational standpoint, compaction bands, like all deformation bands of finite thickness, represent weak discontinuities in the sense that they feature a jump in the displacement gradient field across the band. To accommodate such discontinuities, the standard finite element requires significant enhancements, including for example, frictional contact elements [91, 92], strong discontinuities [12, 13, 60], or extended finite elements [51, 74, 103]. These approaches, however, treat the diffuse deformation bands as a discrete fault (strong discontinuity) with zero thickness, and there is some ambiguity with regards to finding a generally accepted robust algorithm to propagate the discontinuity through the mesh [52, 102]. In addition, the FEM method lacks a characteristic length scale giving rise to spurious mesh discretization sensitivity. The gradient enhanced continuum damage method [19, 26, 27, 76] and the phase-field approach [1, 2, 6, 47, 95] are a promising alternative to propagating deformation bands or fractures in solid continua. Both methods regularize the discontinuous field (whether it be fracture or deformation band) by introducing a diffuse damage zone through a damage or phase

field variable and an internal length scale, rendering the models nonlocal. Although both approaches originate from different mechanical viewpoints, for example, gradient enhanced damage models have their roots in local damage or integral-based nonlocal damage theories [11, 56], and were derived distinctly, they offer considerable similitudes [32], and gradient enhanced damage and phase field methods have the advantage that they propagate discontinuities without the need for arbitrary ad hoc criteria.

An alternative pathway to solve the issue of nonlocality in numerical simulations involving localization of deformation is to possess a characteristic length scale in the discretization technique itself. The smoothed particle hydrodynamics (SPH) method is a meshfree Lagrangian continuum-based method which discretizes a continuum domain into particles that carry continuum properties and fields, and the governing equations are solved over the particles using a kernel-based approximation. The size of the kernel functions is controlled by the smoothing length parameter, which is a numerical characteristic length scale. Thus, the SPH method possesses certain conceptual similitudes to the integral based nonlocality of some continuum damage models. The SPH method has various other additional advantages making its use increasingly popular in geomechanics [23, 24, 44, 45, 75, 107, 108] including its meshfree nature and relative computational efficiency, and is therefore able to handle large deformation simulations. Recent work by the authors has successfully employed the SPH method to model shear band propagation across different geologic settings and spatial scales [34, 36, 38], but to date, SPH has not been used to simulate the phenomenon of compaction band formation.

Recent work using the phase field method [52, 53, 102] exploited principles from past modeling efforts using breakage mechanics 30 42 combined with critical state plasticity to model compaction band formation and propagation in porous rock. Specifically, Ip and Borja 52 developed a degradation function that incorporated the effects of pore collapse mechanisms on both elastic and plastic deformation. Basing themselves on breakage mechanics concepts, they proposed a novel free energy function, where a portion of the compressive free energy is retained even after the material is fully damaged. With a similar goal in mind, in this paper, we develop a new continuum damage model for the SPH method where the damage variable represents the degree of grain crushing in the porous rock, and a degradation function incorporating pore collapse effects is used to capture the sudden onset of pore collapse in the modified Cam Clay (MCC) plasticity model. The proposed damage model capitalizes on the nature of the SPH approximation to propose a kernel-based approximation for the nonlocal equivalent strain that follows naturally from the integral form of nonlocal damage, and we also propose an SPH discretized version of a gradient enhanced damage model. In the latter formulation for SPH, two characteristic length scales arise, and we explore the effects of varying these and also determine the ideal relation linking them. Our model focuses on compaction bands induced by grain crushing and as such, is able to both capture the development of pure and shear-enhanced compaction bands, including hinged-chevron type bands, as well as the transition from high-angled bands to horizontal bands over increasing confining pressure. We highlight that the proposed model can capture compaction bands in homogeneous samples without any predetermined material imperfections, in samples with random heterogeneous material strength, and in samples with and without geometric imperfections (notches).

In what follows, in Section 2 we provide a brief overview of the governing equations and the proposed nonlocal damage model at the continuum scale with its two constituent parts, the mechanical damage model (Section 2.1) and the critical state plasticity model (Section 2.2). This discussion is followed by a short overview of the SPH method, and the discretization of the damage model as well as the different ways in which nonlocality is achieved in our SPH-based formulation in Section 3. Section 4 devoted to showcasing the results of numerical simulations recreating and expanding upon laboratory experiments of different porous rocks, Benthehim sandstone (Section 4.1), Berea sandstone (Section 4.2) and Tuffeau de Maastricht (Section 4.3). Concluding thoughts and ideas for future work are provided in Section 5.

2 Theory

In this paper, we combine damage mechanics with the concept of pore collapse instability to model the formation and propagation of compaction bands in porous rocks. Isotropic damage is modeled through the monotonically increasing scalar damage variable d, which varies between the values of 0 and 1. An undamaged material maintains d = 0, whereas a material is fully damaged at d = 1, which represents a complete loss of stiffness and

integrity. However, the latter does not hold in the context of porous rock in our model, as damage is induced by grain crushing, so d=1 only represents completely crushed rock. The elastic response is degraded through an expression involving the grading index and a postulated degradation function g(d), which is a function of the damage parameter, while the degradation function also affects the plastic behavior of the rock through the evolution equation for the preconsolidation pressure in the MCC model, which we employ to capture plastic behavior. The evolution equation ensures that whenever the porous rock undergoes a grain crushing instability, either softening, perfect plasticity, or hardening can occur. In the event of softening, the preconsolidation pressure decreases while the compaction band forms, and then increases again once grain crushing is complete as a result of the subsequent hardening response.

2.1 Mechanical damage

We consider a standard strain-based damage framework such as that described in [57] 80 where the damage variable d varies with an internal strain history variable κ according to an exponential damage evolution law proposed by Mazars and Pijaudier-Cabot [67],

$$d(\kappa) = 1 - \frac{\kappa_0}{\kappa} \left((1 - a) + a \exp(-b\Delta\kappa) \right), \tag{1}$$

where a and b are material parameters controlling the softening response and $\Delta \kappa = \kappa - \kappa_0 \geq 0$, where κ_0 is an initial threshold value of κ above which damage will initiate. The strain history variable κ is monotonically increasing and represents the maximum possible value obtained by a nonlocal equivalent measure of strain $\bar{\varepsilon}_{eq}$. One possible definition of the local value ε_{eq} of the equivalent strain, adopted in this paper, is the von Mises equivalent strain proposed by de Vree et al. 33 as,

$$\varepsilon_{\text{eq}} = \frac{k-1}{2k(1-2\nu)} I_1 + \frac{1}{2k} \sqrt{\frac{(k-1)^2}{(1-2\nu)^2} I_1^2 + \frac{2k}{(1+\nu)^2} J_2},$$
 (2)

where $I_1 = \operatorname{tr}(\varepsilon)$ and $J_2 = 3\operatorname{tr}(\varepsilon \cdot \varepsilon) - \operatorname{tr}^2(\varepsilon)$ are the invariants of the strain tensor ε , ν is the Poisson's ratio, and k is a parameter that accounts for differing tensile and compressive responses of the material. The nonlocal equivalent strain $\bar{\varepsilon}_{eq}$ is then evaluated at a point of interest \boldsymbol{x} as a weighted average of the local equivalent strains $\varepsilon_{eq}(\varepsilon)$ over the volume V of the domain of nonlocality using the equation [83]

$$\bar{\varepsilon}_{eq} = \frac{1}{V} \int_{V} \omega(\boldsymbol{\xi}) \varepsilon_{eq}(\boldsymbol{x} + \boldsymbol{\xi}) \, dV, \quad \frac{1}{V} \int_{V} \omega(\boldsymbol{\xi}) \, dV = 1,$$
(3)

where $\omega(\xi)$ is a weight function. ξ is a vectorial quantity indicating the relative position of the infinitesimal volume element dV and x. The domain of nonlocality can be either assumed to be a subset of the domain, or the entirety of the domain, see [79]. The strain variables $\bar{\varepsilon}_{eq}$ and κ satisfy the Karush-Kuhn-Tucker conditions [21]

$$\dot{\kappa} \ge 0, \quad \bar{\varepsilon}_{eq} - \kappa \le 0, \quad \dot{\kappa}(\bar{\varepsilon}_{eq} - \kappa) = 0.$$
 (4)

An alternative approach to the integral form of the nonlocal equivalent strain is to develop a gradient formulation from nonlocal theory. Performing the Taylor series expansion for ε_{eq} about the point \boldsymbol{x} as shown by $\boxed{80}$, leads to the following gradient enhanced form of the equivalent strain,

$$\bar{\varepsilon}_{\rm eq} = \varepsilon_{\rm eq} + c_1 \nabla^2 \varepsilon_{\rm eq} + c_2 \nabla^4 \varepsilon_{\rm eq} + \dots$$
 (5)

where ∇^2 is the Laplacian operator, and c_1 and c_2 are coefficients determined by the weight function $\omega(\boldsymbol{\xi})$. Ignoring higher order terms in Eq. [5] leads to,

$$\bar{\varepsilon}_{\rm eq} = \varepsilon_{\rm eq} + l^2 \nabla^2 \varepsilon_{\rm eq},\tag{6}$$

where the parameter $c_1 = l^2$ corresponds to an internal length scale l arising in the gradient formulation. This equation for the nonlocal equivalent strain $\bar{\varepsilon}_{eq}$ differs from the nonlinear expression typically used in finite

element analysis, which results from further differentiating Eq. 5 and rearranging terms (see 80). In SPH, because the kernel function satisfies the C^1 continuity requirements of the displacement field automatically, Eq. 6 is deemed appropriate. An additional requirement of the gradient approach to nonlocal damage is the fulfillment of the Neumann boundary condition,

$$\nabla \bar{\varepsilon}_{eq} \cdot \boldsymbol{n} = 0 \text{ on } \Gamma \tag{7}$$

on every point along Γ , the boundary of the domain in order to solve the partial differential equation in Eq. 6. From the value of d, we can construct a degradation function $g(d) \in [0,1]$ having the following properties: g(0) = 1, g(1) = 0, and g'(d) < 0. A common expression for the degradation function is 52

$$g(d) = (1 - \bar{k})(1 - d)^2 + \bar{k}, \tag{8}$$

where \bar{k} is a stability parameter introduced to avoid singularities. In the context of breakage mechanics, the degradation function g(d) is related to the breakage function B of Einav 42 through the equation

$$g(d) = 1 - B. (9)$$

Unlike in damage mechanics where d=1 implies a completely damaged rock incapable of carrying any load, a completely crushed rock can store an elastic compressive energy albeit at a lower density than the elastic energy that can be stored in an intact rock of the same volume. Einav [42] used statistical homogenization to relate the Helmholtz elastic free energy as a function of breakage B through the equation

$$\psi^e = (1 - B)\psi_0^e + B\psi_u^e \,, \tag{10}$$

where ψ_0^e is the elastic free energy density of an intact rock and $\psi_u^e < \psi_0^e$ is the ultimate elastic free energy of a completely crushed rock.

We can use the degradation function g(d) in lieu of 1-B in Eq. [10]. Equivalently, Ip and Borja [52], [53] defined the grading index θ as

$$\theta = 1 - \psi_u^e / \psi_0^e \,, \tag{11}$$

which represents the crushing potential of the material similar to the grading index defined by Einav $\boxed{42}$. The grading index θ allows the expression of the evolving elastic free energy in terms of the free energy in the uncrushed state, see $\boxed{52}$.

In our model, the following elastic-damage constitutive law relates the Cauchy stress tensor σ to the elastic strain tensor $\varepsilon^{\rm e}$,

$$\boldsymbol{\sigma} = [1 - \theta(1 - g(d))]\mathbb{C}^{e} : \boldsymbol{\varepsilon}^{e}$$
(12)

where \mathbb{C}^{e} is the fourth-order elastic modulus tensor which for an isotropic material is defined as,

$$\mathbb{C}^{e} = K\mathbf{1} \otimes \mathbf{1} + 2\mu \left(\mathbf{I} - \frac{1}{3} \mathbf{1} \otimes \mathbf{1} \right). \tag{13}$$

Here K and μ are the elastic bulk and shear moduli respectively, I is the fourth rank symmetric identity tensor with components $I_{ijkl} = (\delta_{ik}\delta_{jl} + \delta_{il}\delta_{jk})/2$ and I is the second-order identity tensor (Kronecker delta).

The strong form of the initial boundary value problem (IBVP) is posed as follows. On a domain Ω with boundary Γ and Neumann and Dirichlet boundary conditions on $\Gamma_{\tau} \subset \Gamma$ and $\Gamma_{v} \subset \Gamma$ respectively, find the displacement field $\boldsymbol{u}(\boldsymbol{x},t)$ and the nonlocal equivalent strain $\bar{\varepsilon}_{eq}(\boldsymbol{x},t)$ such that:

$$\begin{cases} \nabla \cdot \boldsymbol{\sigma} + \boldsymbol{b} = \rho \dot{\boldsymbol{v}} & \forall \boldsymbol{x} \text{ in } \Omega \times t \\ \dot{\rho} = -\rho \nabla \cdot \boldsymbol{v} & \forall \boldsymbol{x} \text{ in } \Omega \times t \\ \bar{\varepsilon}_{\text{eq}} = \varepsilon_{\text{eq}} + l^2 \nabla^2 \varepsilon_{\text{eq}} & \forall \boldsymbol{x} \text{ in } \Omega \times t \\ \boldsymbol{\sigma} \cdot \boldsymbol{n} = \boldsymbol{\tau} & \text{on } \Gamma_{\tau} \times t \\ \nabla \bar{\varepsilon}_{eq} \cdot \boldsymbol{n} = 0 & \text{on } \Gamma \times t \\ \boldsymbol{v} = \bar{\boldsymbol{v}} & \text{on } \Gamma_{v} \times t \end{cases}$$

$$(14)$$

with initial conditions $\boldsymbol{u}(\boldsymbol{x},0) = \boldsymbol{u}_0$, $\boldsymbol{v}(\boldsymbol{x},0) = \boldsymbol{v}_0$, $\dot{\boldsymbol{v}}(\boldsymbol{x},0) = \dot{\boldsymbol{v}}_0$, $\tau(\boldsymbol{x},0) = \boldsymbol{\tau}_0$, $\bar{\varepsilon}_{eq}(\boldsymbol{x},0) = 0$, $\rho(\boldsymbol{x},0) = \rho_0$, and $\boldsymbol{\sigma}(\boldsymbol{x},0) = \boldsymbol{\sigma}_0$ at time t=0. Here, $\dot{\boldsymbol{v}}$ is the material time derivative of the velocity field, \boldsymbol{b} is the body force (gravity) vector, \boldsymbol{u} is the displacement field vector, \boldsymbol{n} is the unit normal vector to boundary Γ , and $\boldsymbol{\sigma}$ is the total Cauchy stress tensor. Lastly, the vectors $\bar{\boldsymbol{v}}$ and $\boldsymbol{\tau}$ are the prescribed velocity and traction, respectively. The discretization and subsequent solution of this IBVP using the Smoothed Particle Hydrodynamics method is outlined in Section $\boldsymbol{\beta}$. Note that the third equation in Eq. $\boldsymbol{\beta}$ is written here in the form of the gradient damage approach.

2.2 Constitutive Equations

In our elastoplastic continuum damage model, the plasticity model must capture the softening response induced by grain crushing as well as subsequent strain hardening when the crushed grains reach their equilibrium positions. A variation of the original modified Cam Clay (MCC) model is used in this paper. In the MCC model, a yield surface is defined in p-q space, where $p=\text{tr}[\boldsymbol{\sigma}]/3$ is the mean stress (pressure), and $q=\sqrt{3/2}\|\boldsymbol{s}\|$ is the von Mises (deviatoric) stress and $\boldsymbol{s}=\boldsymbol{\sigma}-p\mathbf{1}$ the deviatoric stress tensor.

In p-q space the yield function for the MCC model is an ellipse given by

$$\mathcal{F} = \frac{q^2}{M^2} + p(p - p_c) \le 0, \tag{15}$$

where M is the slope of the critical state line and $p_c < 0$ is the preconsolidation pressure, which determines the diameter of the ellipsoid in the p-axis. M, is defined as,

$$M = \frac{6\sin\varphi_{cs}}{3 - \sin\varphi_{cs}},\tag{16}$$

where φ_{cs} is the critical state internal friction angle of the material. In classical MCC theory [22], the hardening law is given in rate form as

$$\dot{p}_c = -v\varepsilon_v^p p_c, \quad v = \frac{1+e}{\lambda - \tilde{\kappa}},\tag{17}$$

where ε_v^p is the plastic volumetric strain, e is the void ratio, λ is the slope of the virgin isotropic consolidation line, and $\tilde{\kappa}$ is the slope of the swelling line in $\log(p) - e$ space. Note that e and v are assumed to be constant. The elastic moduli,

$$K = [1 - \theta(1 - g(d))]K_0, \quad \mu = \frac{3K(1 - 2\nu)}{2(1 + \nu)}, \tag{18}$$

are treated as constant over Δt , and the Poisson's ratio ν is considered temporally invariant.

The evolution equation from classical MCC theory assumes that the material undergoes stable plastic compaction, which does not hold when the rock grains undergo crushing and the pores collapse. To capture the momentary instability induced by grain crushing, following the argument of [52], the evolution of the preconsolidation pressure is also made a function of the damage variable d in addition to ε_v^p . The participation of d in the evolution law is also done through the degradation function g(d),

$$\dot{p}_c = -v\varepsilon_v^p p_c + g'(d) \frac{\dot{d}}{\lambda_d} \tag{19}$$

where λ_d is a compressibility parameter. The second term in the proposed evolution law is active only during unstable pore collapse resulting from grain crushing, which begins whenever $\varepsilon_v^p = \varepsilon_v^{p*}$ and $p_{c0} = p_{c0}^*$, and is otherwise zero.

We use an associative flow rule to obtain the plastic strain rate,

$$\dot{\boldsymbol{\varepsilon}}^p = \dot{\phi} \frac{\partial \mathcal{F}}{\partial \boldsymbol{\sigma}} = \frac{1}{3} (2p - p_c) \mathbf{1} + \sqrt{\frac{3}{2}} \frac{2q}{M^2} \hat{\boldsymbol{n}}, \tag{20}$$

where $\dot{\phi} \geq 0$ is the plastic consistency parameter and $\hat{n} = s/\|s\|$. Integrating Eq. [19] and the flow rule implicitly, following the steps shown in [38], leads to a variation of the closest point projection (CPP) returning mapping proposed by Borja and Lee [22], which is used to integrate the rate constitutive relations in this paper.

3 SPH Discretization

The smoothed particle hydrodynamics (SPH) method is a continuum Lagrangian particle method that discretizes the continuous problem domain into an assembly of arbitrarily distributed particles over which the governing equations are solved, and which also serve as Lagrangian points carrying continuum-level physical properties of the material such as mass, mass density, stress, and strain. Given a field function f(x,t), where x is the position vector in three dimensions, and t is time, its value for a particular particle at x can be found using the following convolution integral over the support or integration domain \mathcal{B} :

$$\langle f(\boldsymbol{x}) \rangle = \int_{\mathcal{B}} f(\boldsymbol{x'}) W(\boldsymbol{x} - \boldsymbol{x'}, h) d\boldsymbol{x'}.$$
 (21)

Here, W is the kernel or smoothing function which serves as a weighting function, and h is the smoothing length, controlling the size of \mathcal{B} . The kernel function W must satisfy the following three conditions:

$$\int_{\mathcal{B}} W(\boldsymbol{x} - \boldsymbol{x'}, h) d\boldsymbol{x'} = 1, \qquad (22)$$

$$\lim_{h \to 0} W(\boldsymbol{x} - \boldsymbol{x'}, h) = \delta(\boldsymbol{x} - \boldsymbol{x'}), \qquad (23)$$

$$W(\boldsymbol{x} - \boldsymbol{x'}, h) = 0 \text{ when } |\boldsymbol{x} - \boldsymbol{x'}| > k_w h, \qquad (24)$$

where δ is the Dirac-delta distribution and $k_w = 2$ is a constant which defines the radius $k_w h$ of the support domain for the particle. The smoothing length h is a function of the initial inter-particle distance Δ such that $h = k_h \Delta$, and k_h is a constant known as the smoothing length factor. We denote Eq. 22 as the normalization condition, Eq. 23 as the delta function property, and Eq. 24 as the compact support condition. In the SPH method, there is no predefined connectivity between particles, and the interactions between particles are dictated by the kernel function, whose value for a given interaction depends on the normalized distance between the two particles R = |x - x'|/h. In this study we employ the Wendland C^2 kernel,

$$W(R,h) = \begin{cases} \phi_d(1 - R/2)^4 (2R + 1), & \text{for } 0 \le R \le 2, \\ 0, & \text{for } R > 2, \end{cases}$$
 (25)

where the constant ϕ_d takes the values of $\phi_d = 7/4\pi h^2$ in two dimensions and $\phi_d = 21/16\pi h^3$ in three dimensions 104.

The SPH method now approximates the continuous integral of the field function in Eq. 21 as,

$$\langle f(\boldsymbol{x}) \rangle_i = \sum_{j=1}^N f(\boldsymbol{x}_i) W_{ij} V_j,$$
 (26)

and of its first derivative with respect to x as,

$$\langle \nabla f(\boldsymbol{x}) \rangle_i = \sum_{j=1}^N f(\boldsymbol{x}_i) \nabla W_{ij} V_j,$$
 (27)

here $\langle \cdot \rangle$ signifies an approximation, the subscript j corresponds to the neighboring particles of particle i, located at $\boldsymbol{x} = \boldsymbol{x}_i$, $\nabla = (\partial/\partial x, \partial/\partial y, \partial/\partial z)_i$ is the gradient operator, evaluated at the position of particle i, $W_{ij} = W(\boldsymbol{x}_i - \boldsymbol{x}_j, h)$, and $V_j = m_j/\rho_j$ is the volume of particle j, with m_j and ρ_j the mass and mass density of the particle, respectively.

Based on the operators shown in Eqs. 26 and 27, the balance of momentum and mass equations in the IBVP are discretized as follows:

$$\langle \dot{\boldsymbol{v}} \rangle_i = \sum_{j=1}^N m_j \left(\frac{\boldsymbol{\sigma}_i + \boldsymbol{\sigma}_j}{\rho_i \rho_j} \right) \cdot \nabla W_{ij} + \boldsymbol{b}_i,$$
 (28)

$$\langle \dot{\rho} \rangle_i = \sum_{j=1}^N m_j \left(\boldsymbol{v}_j - \boldsymbol{v}_i \right) \cdot \nabla W_{ij}.$$
 (29)

In practical applications due to the dynamic nature of the momentum balance equation (Eq. 28), SPH particles may exhibit oscillations leading to numerical instabilities. We suppress these using a numerical viscosity, namely the Monaghan artificial viscosity [49], which is added into the balance of linear momentum. Hence, the balance of linear momentum becomes

$$\langle \dot{\boldsymbol{v}} \rangle_i = \sum_{j=1}^N m_j \left(\frac{\boldsymbol{\sigma}_i + \boldsymbol{\sigma}_j}{\rho_i \rho_j} + \boldsymbol{H}_{ij} \right) \cdot \nabla W_{ij} + \boldsymbol{b}_i, \tag{30}$$

where Π_{ij} is the artificial viscosity of Monaghan, with coefficients $\alpha_{\pi} = 0.2$ and $\beta_{\pi} = 0.4$.

Next, the nonlocal equivalent strain in integral form can be cast in the context of the SPH approximation, by equating the nonlocal weight function $\omega(\boldsymbol{\xi})$ to the SPH kernel function $W(\boldsymbol{x}-\boldsymbol{x'},h)$ and setting the domain of nonlocality equal to the kernel support domain \mathcal{B} ,

$$\langle \bar{\varepsilon}_{eq} \rangle = \int_{\mathcal{B}} W(\boldsymbol{x} - \boldsymbol{x'}, h) \varepsilon_{eq}(\boldsymbol{x'}) d\boldsymbol{x'} \approx \sum_{i=1}^{N} \varepsilon_{eq}(\boldsymbol{x}_i) W_{ij} V_j.$$
 (31)

A drawback of the integral approach for achieving nonlocality in the equivalent strain, when approximating the integral using the SPH technique, is that the nonlocal domain will always be smaller than the entirety of the domain.

In addition to discretizing the divergence and gradient of field functions, in order to discretize the nonlocal equivalent strain equation (Eq. 6) in the gradient enhanced approach for the nonlocal equivalent strain, there is the need to introduce an operator to discretize the Laplacian of a field function f(x). By taking the Taylor series expansion of a function f_j about x_i up to the third order of accuracy, multiplying both sides by $\frac{x_{ij}}{|x_{ij}|^2} \cdot \nabla W_{ij}$, integrating and then rearranging and performing the SPH approximation of the integral into a summation over particles, the SPH operator for the Laplacian is obtained,

$$\langle \nabla^2 f \rangle_i = 2 \sum_{j=1}^N \frac{m_j}{\rho_j} (f_i - f_j) \frac{\boldsymbol{x}_{ij}}{|\boldsymbol{x}_{ij}|^2} \cdot \nabla W_{ij}.$$
(32)

This SPH operator proposed by [73], has the advantage that it only involves the first derivative of the kernel W, thus avoiding numerical errors that may arise from using the second derivative of the kernel function [24]. While alternative SPH discretizations for the Laplacian have been proposed [43], these generally involve extra computational cost. Additionally, recent work [70]-[72] using this SPH operator for the Laplacian has yielded good results with no significant accuracy loss for large deformation problems involving substantial particle disorder far beyond that sustained in the simulations in this paper. Eq. [6] can now be solved by approximating the Laplacian of the local equivalent strain ε_{eq} ,

$$\langle \bar{\varepsilon}_{eq} \rangle_i = 2l^2 \sum_{j \in \Omega}^N \frac{m_j}{\rho_j} ((\varepsilon_{eq})_i - (\varepsilon_{eq})_j) \frac{\boldsymbol{x}_{ij}}{|\boldsymbol{x}_{ij}|^2} \cdot \nabla W_{ij} + (\varepsilon_{eq})_i.$$
(33)

We note that the summation is performed for $j \in \Omega$ meaning that only the contributions over domain particles are included, and those of the boundary particles are excluded. This exclusion helps to enforce the homogeneous Neumann boundary conditions for the nonlocal equivalent strain $[\Omega]$. A consequence of the gradient approach is the introduction of a constitutive length scale l in addition to the smoothing length h which is a characteristic numerical length scale intrinsic to the SPH method. A relation between the length scales l and h can be obtained by considering the Taylor series expansion of the local equivalent strain $\varepsilon_{\rm eq}$,

$$\varepsilon_{\text{eq}}(\boldsymbol{x}') = \varepsilon_{\text{eq}}(\boldsymbol{x}) + \nabla \varepsilon_{\text{eq}}(\boldsymbol{x}) \cdot (\boldsymbol{x}' - \boldsymbol{x}) + \frac{1}{2} \nabla^{(2)} \varepsilon_{\text{eq}}(\boldsymbol{x}) : (\boldsymbol{x}' - \boldsymbol{x})^{\otimes 2} + \dots
= \sum_{n=0}^{\infty} \frac{h^n}{n!} \nabla^{(n)} \varepsilon_{\text{eq}}(\boldsymbol{x}) : \left(\frac{\boldsymbol{x}' - \boldsymbol{x}}{h}\right)^{\otimes n}
= \sum_{n=0}^{\infty} \frac{(-1)^n h^n}{n!} \nabla^{(n)} \varepsilon_{\text{eq}}(\boldsymbol{x}) : \left(\frac{\boldsymbol{x} - \boldsymbol{x}'}{h}\right)^{\otimes n}$$
(34)

where $\nabla^{(n)}$ is the *n*-th order gradient operator and $(\cdot)^{\otimes n}$ stands for the outer product of *n* vectors [65]. Substituting Eq. [34] into Eq. [31] leads to,

$$\bar{\varepsilon}_{eq}(\boldsymbol{x}) = \int_{\Omega} W(\boldsymbol{x} - \boldsymbol{x}', h) \sum_{n=0}^{\infty} \frac{(-1)^n h^n}{n!} \nabla^{(n)} \varepsilon_{eq}(\boldsymbol{x}) : \left(\frac{\boldsymbol{x} - \boldsymbol{x}'}{h}\right)^{\otimes n} d\boldsymbol{x}'$$

$$= \sum_{n=0}^{\infty} \left(\frac{(-1)^n h^n}{n!} \int_{\Omega} \left(\frac{\boldsymbol{x} - \boldsymbol{x}'}{h}\right)^{\otimes n} W(\boldsymbol{x} - \boldsymbol{x}', h) d\boldsymbol{x}'\right) : \nabla^{(n)} \varepsilon_{eq}(\boldsymbol{x}). \tag{35}$$

It is worth noting that the unity and symmetric properties of the smoothing kernel function W (here the Wendland C^2 kernel function) satisfy the following conditions for arbitrary integer $k \geq 0$:

$$n = 0: \int_{\Omega} W(\boldsymbol{x} - \boldsymbol{x}', h) d\boldsymbol{x}' = 1$$

$$n = 2k + 1: \int_{\Omega} (\boldsymbol{x} - \boldsymbol{x}')^{\otimes n} W(\boldsymbol{x} - \boldsymbol{x}', h) d\boldsymbol{x}' = \mathbf{0}.$$
(36)

Therefore, the Taylor expansion in Eq. 35 can be rewritten as,

$$\bar{\varepsilon}_{eq}(\boldsymbol{x}) = \sum_{\substack{n=2k\\k\geq 0}}^{\infty} \left(\frac{h^n}{n!} \int_{\Omega} \left(\frac{\boldsymbol{x} - \boldsymbol{x}'}{h}\right)^{\otimes n} W(\boldsymbol{x} - \boldsymbol{x}', h) d\boldsymbol{x}'\right) : \nabla^{(n)} \varepsilon_{eq}(\boldsymbol{x})$$

$$= \sum_{\substack{n=2k\\k>0}}^{\infty} A_n \nabla^n \varepsilon_{eq}(\boldsymbol{x})$$
(37)

where

$$A_n \mathbf{1} = \frac{h^n}{n!} \int_{\Omega} \left(\frac{\mathbf{x} - \mathbf{x}'}{h} \right)^{\otimes n} W(\mathbf{x} - \mathbf{x}', h) d\mathbf{x}'.$$
 (38)

Thus, an approximated form of the nonlocal equivalent strain $\bar{\varepsilon}_{eq}$ is obtained as

$$\bar{\varepsilon}_{eq} = \varepsilon_{eq} + A_2 \nabla^2 \varepsilon_{eq} \tag{39}$$

where ∇^2 is the Laplacian operator. A_2 is a linear function of the squared smoothing length (h^2) and can be obtained by solving the integral in Eq. 38 since the kernel function W is known. The value of A_2 given by the Wendland C^2 kernel is

$$A_2 = \begin{cases} \frac{5}{36}h^2, & \dim = 2\\ \frac{2}{15}h^2, & \dim = 3. \end{cases}$$
 (40)

Comparing the form of Eq. 6 and Eq. 39 we see that when taking the gradient length scale $l^2 = A_2$, a second-order approximation of the integral equivalent strain approach is recovered.

Dirichlet-type boundary conditions are enforced through so-called dummy boundary particles, where three to four layers of SPH boundary particles are positioned to represent physical solid walls. The dummy particles

are either fixed in space or move with a prescribed velocity, with their stresses determined from those of the nearby domain particles following the strategy presented in [109], while the density and the mass of the dummy particles are kept fixed throughout the simulation. To avoid the problem of kernel truncation at boundaries when computing the balance of linear momentum, the balance of mass, or the velocity gradient, the boundary particles are used to complete the kernel.

Enforcing traction-type Neumann boundary conditions, which are used to provide confinement along the lateral boundaries in biaxial or triaxial tests, can be laborious in SPH, as it requires determining particles along the free surfaces subjected to confining stresses, the normal vectors for said particles, and the surface area at each particle where the confining stress is applied [82]. A simpler alternative is to employ the flexible confined boundary conditions proposed by Zhao et al. [112], where a confining stress σ_c is applied directly to the conservation of momentum equation (Eq. [28]), to all the domain particles,

$$\langle \dot{\boldsymbol{v}} \rangle_i = \sum_{j=1}^N m_j \left(\frac{\boldsymbol{\sigma}_i + \boldsymbol{\sigma}_j}{\rho_i \rho_j} + \boldsymbol{\Pi}_{ij} \right) \cdot \nabla W_{ij} + \sum_{j=1}^N m_j \left(\frac{(\sigma_c)_i + (\sigma_c)_j}{\rho_i \rho_j} \right) \nabla W_{ij} + \boldsymbol{b}_i. \tag{41}$$

Using the properties of symmetry and compactness of the SPH kernels and the fact that the kernels of particles along the free surfaces are truncated, it is possible to show that σ_c is applied only at the free surface and vanishes at all other particles within the domain [112]. Therefore, the confining pressure is applied without needing to identify particles along the traction-subjected free surfaces, their normals, or the associated surface areas, significantly reducing computation time and increasing accuracy in the wake of large deformations.

The simulation is evolved dynamically and explicitly in time using a semi-implicit time integration scheme $\boxed{100}$. In this scheme, the particle velocity is updated first, followed by its position and density, while the time step, $\Delta t = t_{n+1} - t_n$, is selected to satisfy the Courant–Friedrichs–Lewy (CFL) condition to ensure the stability of the simulation:

$$\Delta t = C_0 \frac{h}{c_s},\tag{42}$$

here C_0 is the CFL coefficient, taken as 0.1, and $c_s = \sqrt{E_0/\rho_0}$ is the numerical sound speed of the material, where E_0 and ρ_0 are the reference elastic modulus and mass density of the material, respectively. In this paper, the continuum elastoplastic damage model is implemented into the parallel SPH code GEOSPH [36], [38] built on the open-source framework PySPH [85], which we use to perform the simulations shown in Section [4]. For further details regarding the code and its implementation, the reader is referred to [34], [35].

4 Numerical Examples

The continuum elastoplastic damage model developed for SPH is evaluated by simulating experimental tests on three different types of porous sedimentary rock. Specifically, we consider porous sandstones such as those from the Bentheim and Berea formations in Germany and the Midwestern part of the United States respectively, in addition to Tuffeau de Maastricht, a soft and highly porous calcarenite (limestone) from the Netherlands with weak cementation between the constituent grains. The sandstone rocks are generally made of quartz and feldspar, with lesser quantities of clay minerals, whereas the calcarenite is predominantly calcite (> 90%) with a smaller clay content. Despite their differing mineralogical composition, these three types of rock are known for displaying compaction localization as a result of pore collapse and grain crushing. Additionally, they are known for their potential for use as a reservoir rock, either for the extraction of water for geothermal energy projects 46, for hydrocarbon extraction, or as host rocks for CO₂ sequestration. In what follows we perform plane-strain biaxial simulations to evaluate and demonstrate the capabilities of our elastoplastic damage model in SPH against experimental results provided by Tembe et al. 96 and Leuthold et al. 58. We observe several features consistent with the experimental results, including softening behavior after localization and subsequent hardening, similar stress-strain responses to experimental results, and a transition from high-angle bands to horizontal compaction bands as the confining pressure increases. We also explore the properties of the smoothing length parameter h, the role of the additional constitutive damage length scale l, and the nonlocality stemming from SPH as well as the gradient enhanced damage approach. Lastly, the effects of geometric differences between notched and notchless samples are discussed.

4.1 Bentheim Sandstone

A number of numerical simulations of biaxial compression tests of Bentheim sandstone samples are performed to observe compaction band formation under confining pressure. The Bentheim sandstone sample has a height of 38.1 mm, a width of 18.4 mm, and two V-shaped notches on the sides with a height and width of 2 mm, resulting in a slightly narrower sample neck at mid-height, modeled after the geometry used in the laboratory experiments performed by Tembe et al. $\boxed{96}$. The specimen is subjected to a confining pressure σ_c of -250 MPa, and is compressed vertically downwards at the top at a velocity of 0.1 mm/s (within the experimentally known quasistatic range of deformation in SPH [101]) and has a fixed bottom boundary. The sample is compressed until a maximum axial strain of $\gamma_a = 1.8\%$ is reached. The top and bottom surfaces of the sample are enveloped by boundary particles, and the lateral sides are left as free surfaces where we apply the confining pressure using the flexible confining boundary conditions approach. The material parameters of the simulations are as follows: the Young's modulus is E = 19.2 GPa, Poisson's Ratio is $\nu = 0.27$, the initial density is $\rho_0 = 1980$ kg/m^3 , the critical state line slope is M = 1.2, the void ratio is e = 0.2953, the initial preconsolidation pressure is $(p_c)_0 = -420$ MPa, the grading index is $\theta = 0.88$, the damage parameters k, a, and b are 10, 1, 380, respectively, the isotropic consolidation index is $\lambda = 0.12$, the swelling index is $\tilde{\kappa} = 0.07$, and the compressibility parameter is $\lambda_d = 2.2$. The threshold strain variable is set to $\kappa = 1.2$ e-4. The initial interparticle distance is $\Delta = 0.5$ mm, the smoothing length factor is $k_h = 1.5$, and a total of 3536 particles are used in the model discretization.

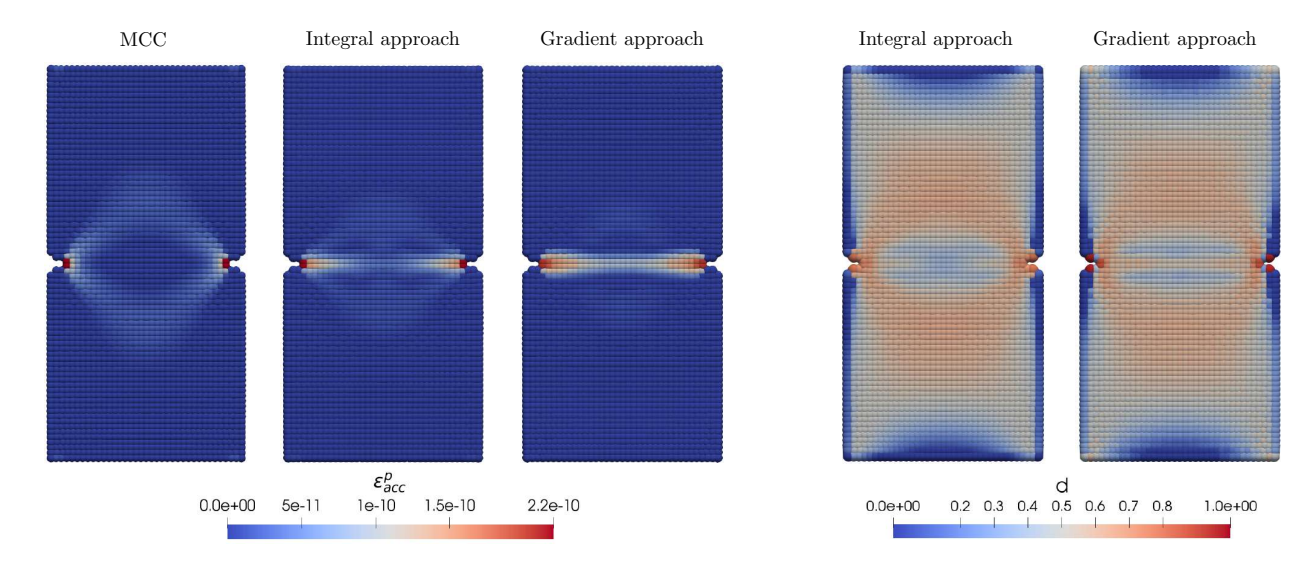


Fig. 1. Comparison of the integral and gradient enhanced elastoplastic damage models, with results from a MCC elastoplastic model shown as a point of reference for the Bentheim sandstone samples and $\sigma_c = -250$ MPa. On the left, contours of the accumulated plastic strain ε_{acc}^p , and on the right, contours of the damage variable d are shown.

In the first series of simulations displayed in Figure \square we compare the results of the biaxial test between the integral elastoplastic damage approach and the gradient enhanced elastoplastic damage approach setting $l^2 = \frac{5}{36}h^2$ to ensure that the gradient enhanced model is exactly a second-order approximation. In addition, we include the results of a basic elastoplastic model only involving the MCC model and no damage, as a point of reference. Contours of the accumulated plastic strain ε_{acc}^p displayed on the left side of the plot, indicate that the basic MCC model can only simulate a diffuse chevron-like plastic strain zone, and is unable to capture a localized compaction band as evident in the gradient and integral approach simulations. The integral and

gradient approaches correctly capture a localized horizontal zone of grain crushing, oriented perpendicular to the maximum compressive stress, mirroring the experimental results of Tembe et al. $\boxed{96}$. However, the integral approach produces a compaction band of somewhat lower magnitude accumulated plastic strain throughout the central zone of the band. Similar results are observed in terms of the damage variable d on the right-hand side of the plot, although the damage and therefore the amount of grain crushing is considerably more diffuse than the accumulated plastic strain, indicating a damaged zone that extends past the narrowed strip between the notches. In the thin sections presented in $\boxed{96}$, grain crushing was also observed to surpass the sample neck region. Discrepancies between the integral and gradient approaches are expected, as the gradient approach is an approximation of the integral approach.

We note that both the integral and gradient damage approaches generate a secondary zone of localized plastic strain and deformation surrounding the compaction band area, emanating from the notches as seen in Figure 1. These lower magnitude and more diffuse zones are oriented roughly at an angle of approximately 45° to the horizontal and are in fact shear-enhanced compaction bands, falling within the 38° to 53° orientation with respect to the principal stress direction, and exhibiting a sharp 90° hinge between the deformation bands, typical of chevron-type shear-enhanced compaction bands 10, 41.

One advantage of the SPH method is the intrinsic numerical nonlocality stemming from the kernel approximation and the smoothing length h which can be taken advantage of to achieve discretization-independent solutions, for example as manifested in terms of the width of the localization zones [99]. Such capabilities contrast with mesh-based methods such as the conventional finite element method which is well known to suffer from pathological mesh sensitivity associated with strain softening and localization. Discretization-independent results are possible in the SPH method even while using a constitutive model that is not equipped with a characteristic length scale, as occurs in the integral nonlocal damage approach when setting the domain of nonlocality equal to the kernel support domain [34], as long as the smoothing length is kept fixed as the discretization is varied (by changing the initial interparticle distance Δ). Therefore, with a priori knowledge of the experimental shear band thickness, the smoothing length can be adjusted to accommodate this desired thickness. From Figure Π a smoothing length of h = 0.75 accurately captures the experimentally observed compaction zone width across the sample neck between the notches, so it is used in the following sensitivity analysis (Figure 2), where the interparticle distance and the smoothing length factor are varied while ensuring the smoothing length $h = k_h \Delta$ is constant. In total four simulations are performed, the first with $\Delta = 0.55$ mm, $k_h = 1.\overline{36}$, and 2855 total particles, the second with $\Delta = 0.5$ mm, $k_h = 1.5$, and 3536 particles (like in Figure 1), the third with $\Delta = 0.4$ mm, $k_h = 1.875$, and 5496 particles, and the fourth with $\Delta = 0.3$ mm, $k_h = 2.5$, and 9712 particles.

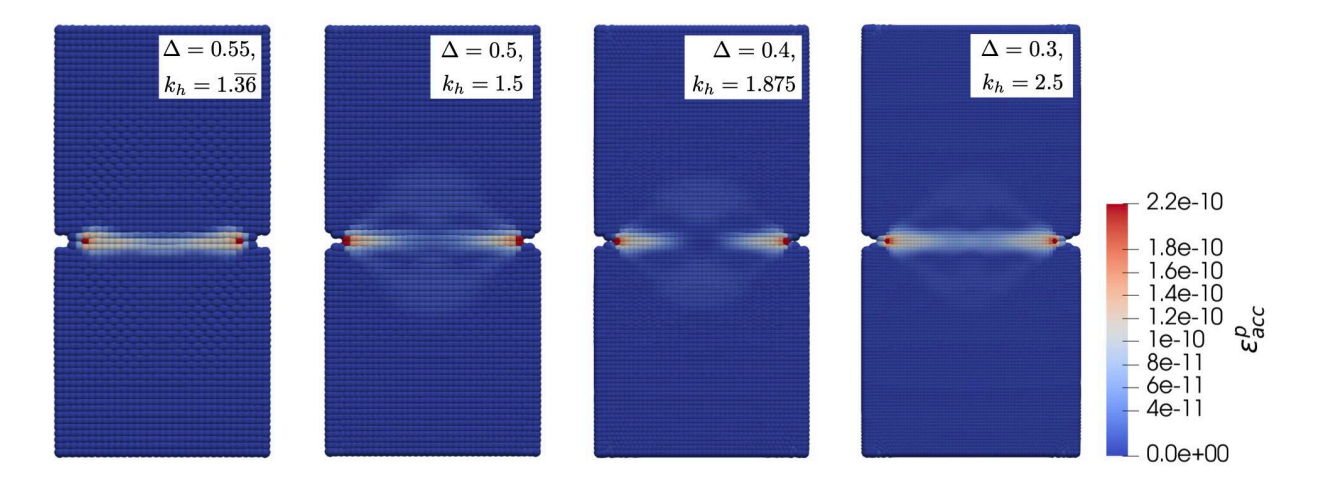


Fig. 2. Sensitivity analysis of biaxial tests performed on Bentheim sandstone showing contours of the accumulated plastic strain ε_{acc}^p . The smoothing length is fixed $h = k_h \Delta = 0.75$ while the discretization level is changed.

The width of the compaction bands generated by each of the different discretizations is quantitatively measured by fitting a Gaussian function to the accumulated plastic strain across the neck of the sample, and defining the full width at half maximum of the Gaussian $2\sqrt{2\ln(2)}SD$, where SD is the standard deviation of the Gaussian, to correspond to the localization zone width [86]. The width of the compaction band w is taken as the average of three different measurement locations along the band. In Figure [3], the fitted Gaussians at one such cross section at x=-6 mm (where x=0 mm is at the midpoint in the horizontal direction) are displayed showing almost no perceivable difference in the fitted Gaussians and compaction band thicknesses. The determined widths at half maximum for the Gaussian are w=0.57 mm for $\Delta=0.55$ mm and $k_h=1.36$; w=0.60 mm for $\Delta=0.5$ mm and $k_h=1.5$; w=0.61 mm for $\Delta=0.4$ mm and $k_h=1.875$; and w=0.65 mm for $\Delta=0.3$ mm and $k_h=2.5$. Although the measured thicknesses of the compaction bands are very close, there are small discrepancies in the magnitude of the accumulated plastic strain, as well as the omission of a secondary, diffuse, chevron-like crushing zone surrounding the localized horizontal band in the $\Delta=0.55$ mm and $k_h=1.5$ satisfactory while being computationally efficient due to the smaller number of particles, and we use this level of discretization going forward.

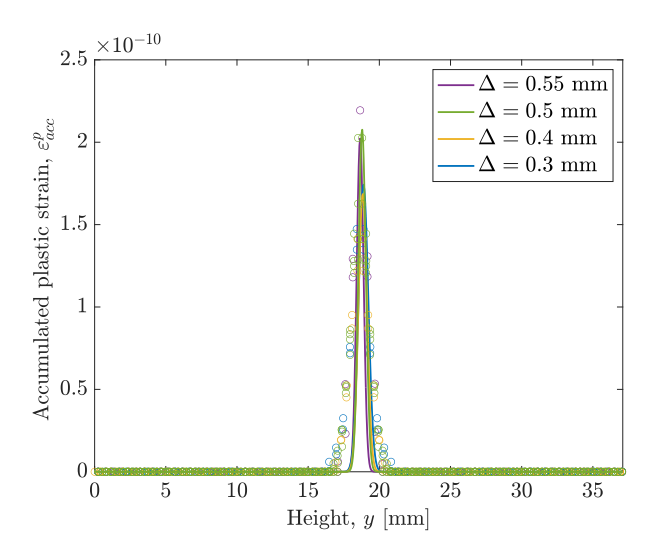


Fig. 3. Gaussian functions fitted to the accumulated plastic strain across the horizontal compaction band for the different simulations performed as part of the sensitivity analysis shown in Figure 2 measured at x = -6 mm.

While keeping the constitutive characteristic length scale parameter l in the gradient damage approach fixed at $l^2 = \frac{5}{36}h^2$ ensures the closest possible approximation to the integral approach, l can be varied in its own right to smoothen or further localize the deformation bands. This feature can be advantageous, as it enables smoothing without increasing h and the kernel radius, leading to an increased number of neighboring particles and computational cost. In Figure 4 five different simulations are conducted varying l as a function of the initial interparticle distance Δ , with $h = k_h \Delta = 0.75$ maintained constant. As can be seen, increasing l visibly augments the region of grain crushing away from the sample neck area extending further afield, and by $l = 3.0\Delta$, the localized compaction band has been mostly dissipated into a much more diffuse region of crushing. The widths of the compaction bands are measured by the previously mentioned procedure, using the full width at half maximum of Gaussian functions fitted to ε_{acc}^p . For $l = 0.5\Delta$, w = 1.25 mm; for $l = \Delta$, w = 1.24 mm; for $l = 1.5\Delta$, w = 1.59 mm; for $l = 2.0\Delta$, w = 2.49 mm; and for $l = 3.0\Delta$, w = 10.53 mm.

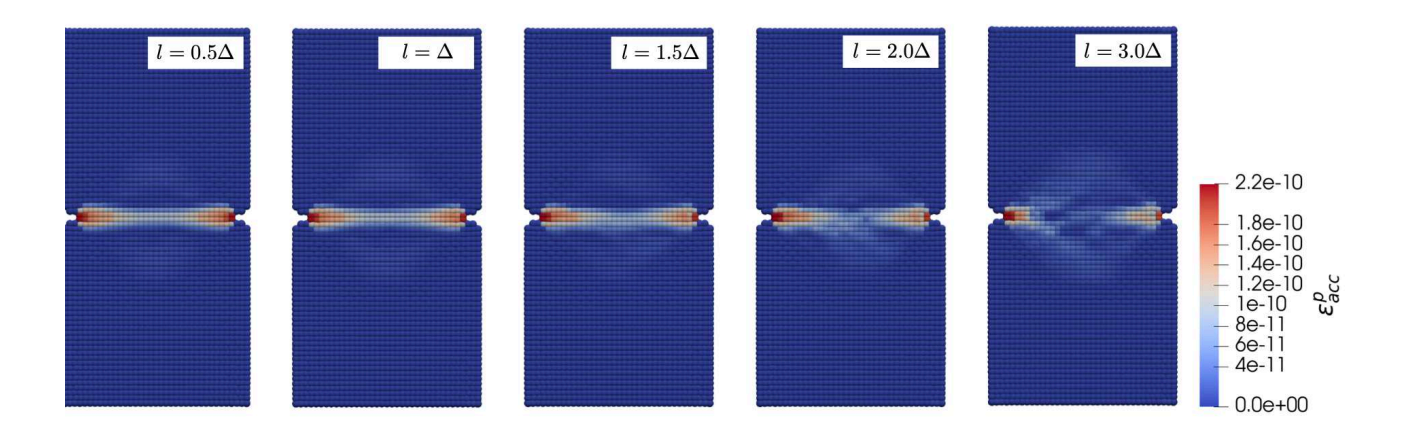


Fig. 4. Contours of the accumulated plastic strain ε_{acc}^p for biaxial simulations of Bentheim sandstone given different values of l the constitutive characteristic length scale originating from the gradient damage approach formulation.

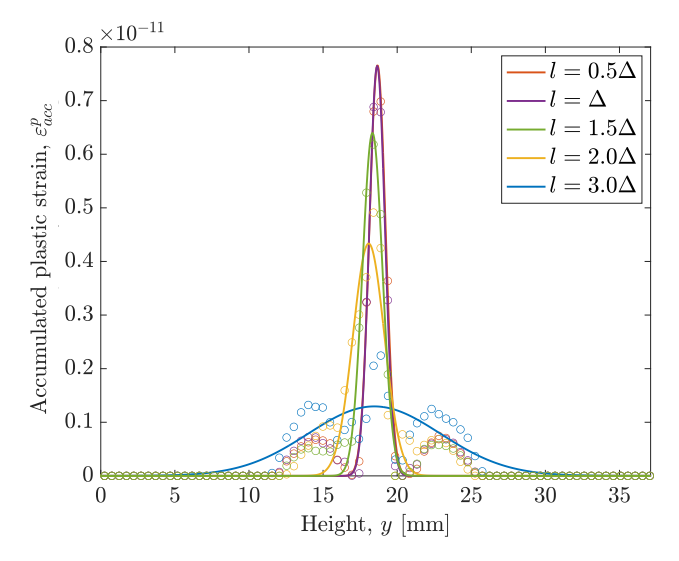


Fig. 5. Gaussian functions fitted to to the accumulated plastic strain at the cross section taken at x=0 for biaxial Bentheim sandstone tests with different values of l. Note the fitted Gaussians for $l=0.5\Delta$ and $l=\Delta$ appear superimposed due to their similarity.

As seen from the essentially indistinguishable contour plots of ε_{acc}^p and the very similar compaction band widths between the $l=0.5\Delta$ and $l=\Delta$ simulations, the gradient constitutive length scale l is only able to significantly influence the localization width for $l\geq \Delta$, and assigning $l<\Delta$ will have no tangible effect on the simulation results. We observe another advantage of the gradient enhanced model, which is that additional localization of deformation bands can be obtained by reducing l up to $l=\Delta$, without needing to decrease the

smoothing length h. This fact helps to avoid a potential loss of accuracy that would occur with a small h, as the accuracy of the SPH solution depends on having a sufficient number of particles within the support domain 65.

A similar conclusion can be drawn from the plot of axial force against axial strain from the same biaxial tests (Figure 6), as the $l=0.5\Delta$ and $l=\Delta$ simulations display practically indistinguishable force-strain responses. In general, the axial force-strain relations determined from the SPH simulations behave reasonably well compared to experimental results from Tembe et al. 96, even up to $l=2.0\Delta$, where the compaction band is more diffuse than that observed in the experimental results. Shortly after a peak force is obtained, grain crushing occurs prompting the propagation of the compaction band and the onset of softening behavior followed by hardening. The experimental results indicate that softening occurs over shorter temporal intervals, which may result from multiple distinct deformation band propagation events across the sample neck, ultimately coalescing into one distinct band, but the subsequent hardening ensures the final axial force is similar in both experiment and simulation. For $l=3.0\Delta$ however, the highly diffuse nature of the grain crushing zone, and its temporally slightly later development lead to an overprediction of the axial force and an insufficient softening response. We stress that the simulation with the value of $l=3.0\Delta$ is for illustrative purposes only, to highlight the potential effects of negligent manipulation of this constitutive length scale parameter, and conclude that l has a relatively minor role in impacting the force-strain curve as long as the degree of smoothing does not inhibit the development of a narrow compaction band.

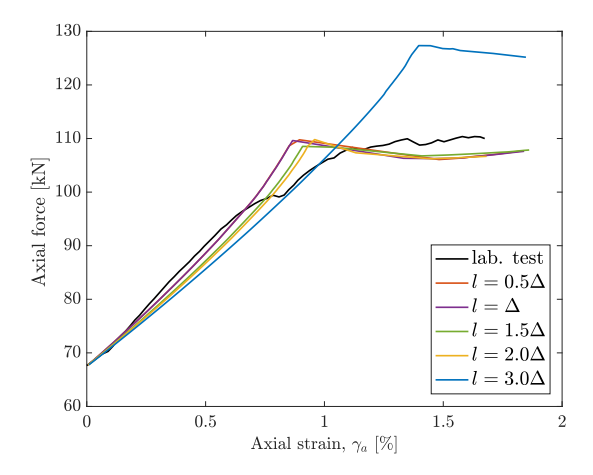


Fig. 6. Axial force as a function of axial strain for the different biaxial simulations performed with varying length scales l for Bentheim sandstone. Results are compared against the experimental laboratory test performed by 96.

In Figure 7 the effect of the grading index θ on the development of compaction bands is explored. All our simulations here use the integral nonlocal damage approach, and the same parameters as the other Bentheim simulations with the exception of θ . Contours of the accumulated plastic strain demonstrate that increasing the grading index from 0.86 to 0.88 (the calibrated value for the previously shown Bentheim sandstone tests) and then to 0.9 concentrates the zone of crushing into a more narrow compaction band. At $\theta = 0.86$ low-angle chevron-type shear-enhanced compaction bands form. At $\theta = 0.88$, a main compaction band propagates in the sample neck and is accompanied by secondary shear-enhanced compaction bands in a chevron-type configuration. These secondary chevron bands disappear with a slight increase in the grading index to $\theta = 0.9$, where only a compaction band going through the sample neck is produced. These results confirm the observations of Ip and Borja 52, indicating that θ may be an additional factor controlling the degree of localization in the deformation bands, and also the type of deformation band observed.

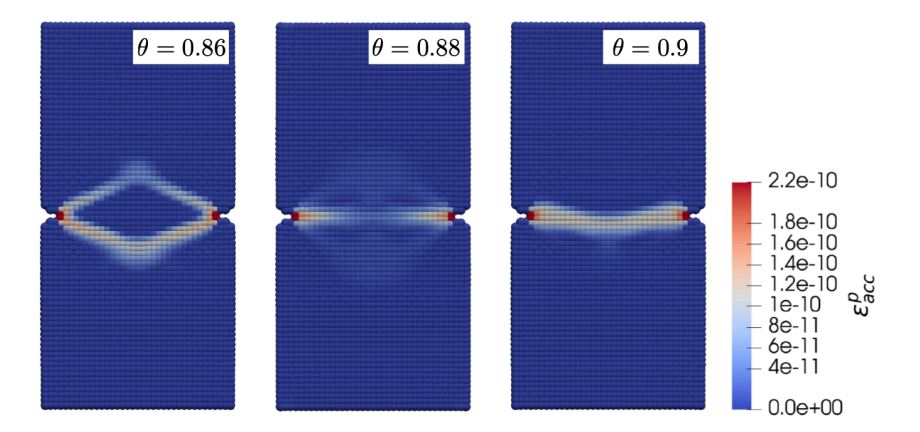


Fig. 7. Contours of the accumulated plastic strain ε_{acc}^p for biaxial simulations given different values of the grading index θ . Results shown at the final axial strain. Here the integral damage model was used.

4.2 Berea Sandstone

Three simulations of Berea sandstone, involving notched specimens of the same dimensions as in Section 4.1 are performed with the confining pressures of -150, -200, and -250 MPa with SPH using our proposed damage model. The results are compared against the laboratory tests of Tembe et al. $\boxed{96}$. The simulations have the same setup as those performed on the Bentheim sandstone, including the discretization, boundary conditions, and loading rate. The simulations are conducted until a final axial strain of $\gamma_a = 2.1\%$ is reached. The elastic moduli of the Berea sandstone are E = 9.24 GPa and $\nu = 0.25$, and the initial density is $\rho_0 = 2100$ kg/m³. The plastic parameters of the critical state model are M = 1.05, the void ratio e = 0.2658, an initial preconsolidation pressure $(p_c)_0 = -400$ MPa, the grading index is $\theta = 0.85$, the isotropic consolidation index is $\lambda = 0.21$, the swelling index is $\tilde{\kappa} = 0.016$, and the compressibility parameter is $\lambda_d = 2.5$. The damage parameters are k, k, and k are 15, 1, 385, respectively, while the threshold strain variable is k = 1.4e-4. Like in the Bentheim simulations, the initial interparticle distance k is set to k = 0.5 mm, the smoothing length factor is k = 1.5, and a total of 3536 particles are used in the model discretization. In all the simulations performed on the Berea sandstone displayed in this subsection, the integral form of the nonlocal damage is used.

The final configurations of the biaxial test simulations performed at the three levels of confining pressure are shown in Figure 8 displaying contours of the damage variable. The simulations are able to replicate the damage patterns produced in the experimental study by Tembe et al., visualized through the use of optical microscopic thin sections, involving two distinct conjugate chevron-like shear-enhanced compaction bands. In both experiments and simulations, the neck zone between the notches remains relatively undamaged, and in the lower confining stress simulations $\sigma_c = -150, -200$ MPa, the width of the bottom-most band is slightly thicker. Like in the experiments, the overall thickness of the zone of grain crushing reduces in width with increased confining pressure. Tembe et al., found the inclination of the conjugate bands to be inclined on average at angles of 55° to the principal stress direction, and in our simulations, we obtain similar values, 53.3° for $\sigma_c = -150$ MPa, 58.8° for $\sigma_c = -200$ MPa, and 61.2° for $\sigma_c = -250$ MPa at the conclusion of loading.

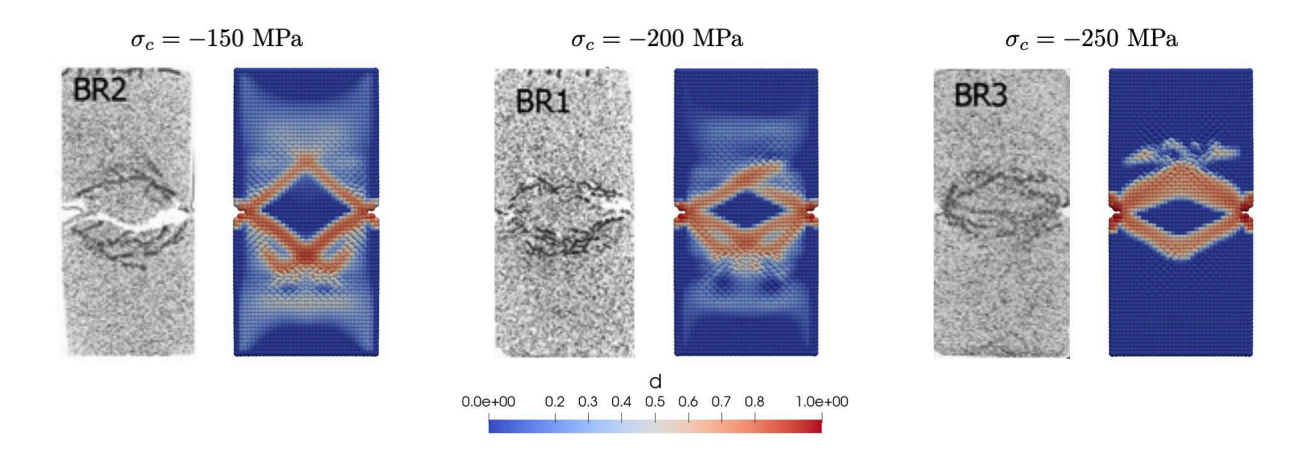


Fig. 8. Comparison of optical microscopic thin sections from Tembe et al. [96] showing spatial distribution of damage with damage variable d contours from our SPH simulations at varying confining stress σ_c . All snapshots are shown at the final axial strain of $\gamma_a = 2.1\%$. All simulations performed with the integral damage model.

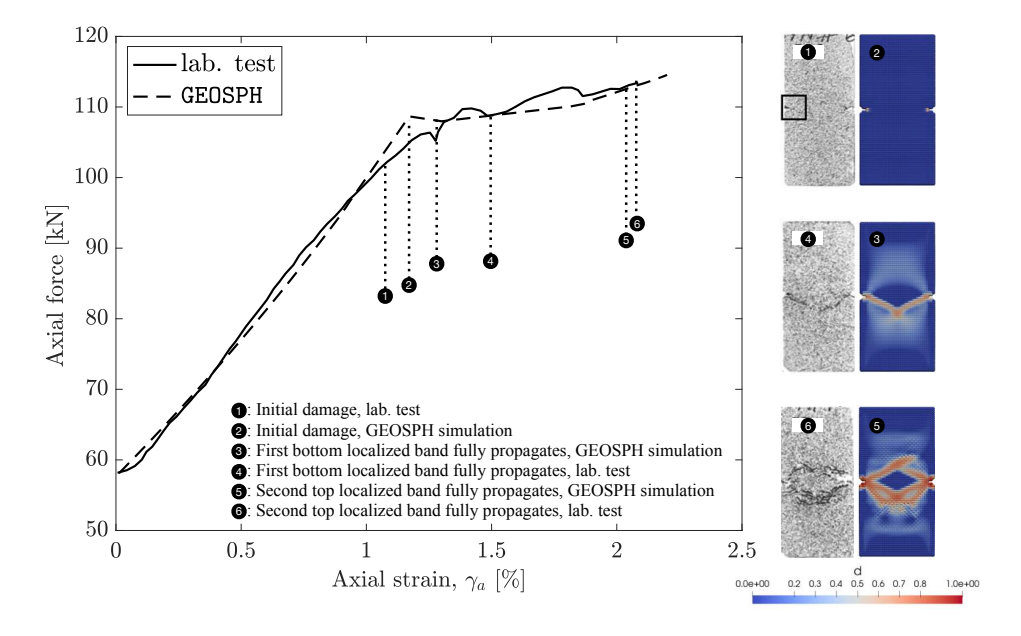


Fig. 9. Axial force as a function of axial strain compared between the laboratory test performed on Berea sandstone by 96, and our biaxial simulations conducted with GEOSPH given $\sigma_c = -200$ MPa. On the right-hand side, optical microscopic thin sections showing the initiation of damage as well as the subsequent propagation of localized damage zones are compared with contours of the damage variable from the SPH simulations. Numbers circled in black indicate the amount of axial strain at which the snapshots on the right-hand side are displayed.

In Figure \mathfrak{D} , the axial force is plotted as a function of the axial strain for both the laboratory test of Tembe et al., as well as in the equivalent SPH simulation given a confining stress of $\sigma_c = -200$ MPa. On the right side, snapshots at different axial strains showcase the development of zones of localized damage both in the

experiments and in our simulations. We observe that the numerical simulations accurately model the forcestrain history of the experiments, as well as the propagation sequence of the deformation bands, with damage occurring first at the notches, followed by the formation of an initial shear-enhanced compaction band below the sample neck, and then the development of a second conjugate shear-enhanced compaction band above the sample neck. At the end of the test, two shear-enhanced compaction bands forming chevron patterns are visible. We note that the force-strain curves for both simulation and experiment show a relatively shortened softening response after the initial force peak as the first band finishes propagation, and hardening rapidly ensues.

4.3 Tuffeau de Maastricht

We next conduct plane-strain biaxial simulations on Tuffeau de Maastricht, a highly porous limestone rock, mimicking the laboratory tests performed by Leuthold et al. [58], to discern the role of the confining pressure σ_c in determining the predominant deformation mode within the sample. The computational sample dimensions were taken as a rectangular specimen of 140 mm height and 70 mm width discretized with an initial interparticle distance of $\Delta=2.0$ mm resulting in a total of 2730 particles in the discretization. Unlike the Bentheim and Berea simulations, there is no notch in the rock sample geometry. Similar to the Bentheim sandstone simulations, however, the top and bottom of the sample were surrounded by boundary particles, and the lateral boundaries were left free to apply the confining pressure. A downward vertical velocity of 0.1 mm/s was applied to the top boundary particles to compress the simulation until the desired maximum axial strain was obtained (this amount depended on the value reported in the experimental data). In total seven simulations were performed with different values of the confining pressure, $\sigma_c=-1.0, -1.5, -2.5, -3.25, -4.0, -5.0$, and -6.0 MPa, in accordance with the available experimental testing [58]. The material and SPH parameters used in the simulations are reported in Table [1]. Note, the integral damage approach was utilized in these simulations.

Parameter Value Initial interparticle distance, Δ [mm] 2.0 Smoothing length factor, k_h 1.5 Soil specimen width, W [mm] 70 Soil specimen height, H [mm] 140 Compaction velocity, V [mm/s] 0.1Initial density, ρ [kg/m³] 1700 Young's modulus, E [GPa] 1 Poisson's Ratio, ν 0.14Critical state line slope, M1.65 Void ratio, e1.096 0.1 Virgin isotropic consolidation index, λ |0.021|Swelling index, $\tilde{\kappa}$ Initial preconsolidation pressure, $(p_c)_0$ [MPa] -6.7Grading index, θ 0.9 Initial mean stress (confining pressure), $p_0 = \sigma_c$ [MPa] -1.0, -1.5, -2.5, -3.25, -4.0, -5.0, -6.0Threshold strain variable, κ 2.0e-4 $k \text{ in } \varepsilon_{\text{eq}}$ 10 a in calculating d1 b in calculating d390 Compressibility parameter, λ_d 1.0

Table 1. Biaxial test simulation parameters: Tuffeau de Maastricht.

Figure 10 presents results of the biaxial test under a confining pressure of $\sigma_c = -2.5$ MPa, and the deviatoric stress q is plotted against the axial strain γ_a . On the right-hand-side panels of the figure, contours of the damage variable are displayed, capturing the evolution of a high-angle localized shear-enhanced compaction band which emanates jointly from the top middle and the top left corner of the sample coalescing and then propagating across the sample, as well as a second band which propagates from the bottom left corner. The first band shown

in snapshot (1) at $\gamma_a=1.09\%$, nucleates right after the stress peak and is responsible for a substantial drop in the stress, and is quickly followed by the second band emanating from the bottom left corner as depicted in (2) at $\gamma_a=1.11\%$. The minimum in the deviatoric stress is achieved at $\gamma_a=3.36\%$ at which point both bands have finished propagating. Subsequently, for the remainder of the simulation, the shear-enhanced compaction bands continue to grow in width and the stress-strain curve displays evidence of material hardening. We see that the stress-strain curve determined from the laboratory testing shows a reduced softening response, but overall, it shows similar behavior to our SPH simulations including close peak and ultimate stresses.

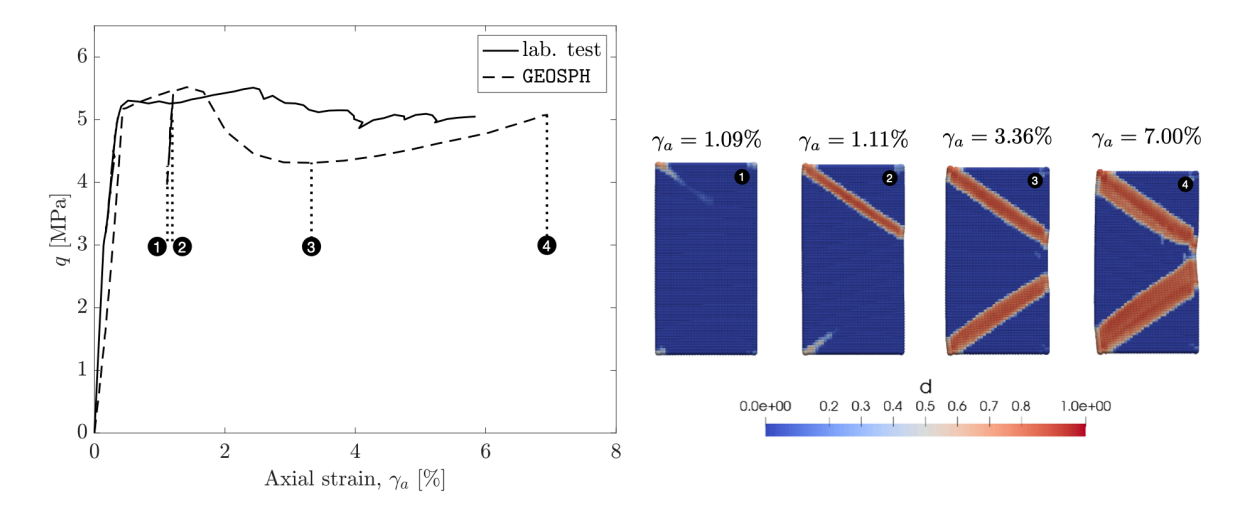


Fig. 10. (left) deviatoric stress q as a function of axial strain γ_a for the simulation performed by GEOSPH and from the laboratory test performed by 58 given $\sigma_c = -2.5$ MPa. (right) contours of the damage variable d at different values of the axial strain. Note that the contours of the accumulated plastic strain ε_{acc}^p show identical patterns to those of the damage variable d and are therefore omitted. Numbers circled in black indicate the amount of axial strain on the stress-strain plot at which the snapshots on the right-hand side are displayed.

While the continuum damage framework presented in this paper does not rely on the theory of bifurcation to predict and numerically propagate localized damage or deformation bands, bifurcation theory can be used to interpret and help explain the orientations and types of deformation bands forming in the porous limestone rock. Since the elastoplastic constitutive tensor \mathbb{C}^{ep} will not be identical inside and outside the deformation band due to the damage-induced degradation, the following condition describing discontinuous bifurcation must be used to detect the onset of localization [30] [88],

$$\det(\mathbf{A}) < 0 \tag{43}$$

where $\det(\cdot)$ is the determinant operator and \boldsymbol{A} is the second-order acoustic tensor expressed as,

$$\mathbf{A} = \mathbf{n} \cdot \mathbb{C}^{\mathrm{ep}} \cdot \mathbf{n}. \tag{44}$$

Here n is the normal vector indicating the localization band orientation, characterized under plane-strain conditions in terms of the angle α between the normal and the horizontal,

$$n_i = \begin{bmatrix} \cos(\alpha) \\ \sin(\alpha) \\ 0 \end{bmatrix} \tag{45}$$

for i=x,y,z, with x the horizontal, y the vertical axes, and z into the page. The elastoplastic constitutive tensor is a function of the fourth-order elastic modulus tensor \mathbb{C}^{e} ,

$$\mathbb{C}^{\text{ep}} = [1 - \theta(1 - g(d))]\mathbb{C}^{\text{e}} - \mathbb{C}^{p} = [1 - \theta(1 - g(d))] \Big(\mathbb{C}^{\text{e}} - \frac{1}{\chi}\mathbb{C}^{\text{e}} : \mathbf{G} \otimes \mathbf{F} : \mathbb{C}^{\text{e}}\Big), \quad \chi = \mathbf{F} : \mathbb{C}^{\text{e}} : \mathbf{G} + H$$
(46)

where for an associated flow rule, $F = G = \partial \mathcal{F}/\partial \sigma$ and H is the plastic modulus 14, 17.

In Figure $\boxed{11}$ the normalized determinant of the acoustic tensor is plotted as a function of the localization band orientation angle α for various points in time corresponding to different amounts of axial strain γ_a , ranging from $\gamma_a = 0.85$ to 1.1%, in order to monitor the evolving localization viability in the $\sigma_c = -2.5$ MPa simulation. Specifically, the particle that first shows accumulated strain and localized damage/grain crushing near the top center in the first emerging deformation band is selected to plot the determinant of the acoustic tensor. The chosen temporal range corresponds slightly before and after initial yielding at the chosen particle. Orientation angles that correspond to zero or negative values of the normalized determinant indicate the potential formation of localization at that angle value. As discussed by Das et al. $\boxed{29}$ $\boxed{31}$, band inclinations correspond to the orientation angle producing the minimum value of the normalized determinant of the acoustic tensor, due to the principle of maximum dissipation as the orientation rendering the smallest value of the acoustic tensor will produce the weakest plane for deformation to localize.

As seen by the provided plot, prior to yielding the normalized determinant of the acoustic tensor is well above zero, but rapidly approaches zero with increased axial strain. Just prior to yielding, the minimum of $\det(A)/\det(A_e)$ is found to correspond to $\alpha=0^{\circ}$, or horizontal orientation, and then the determinant continues to decrease achieving a minimum value at $\alpha=\pm 34.0^{\circ}$ which is roughly maintained until yielding is reached and the deformation band finishes propagating, resulting in a high-angle shear-enhanced compaction band forming across the top half of the sample. The normalized determinant then increases slightly overall, while retaining a minimum below zero around $\pm 45.0^{\circ}$, only to significantly increase above zero to progressively more positive values, as hardening occurs, indicating reduced potential for localization (omitted from the figure for clarity purposes). We see that the orientation of the deformation bands captured by the damage contours (which match those of the accumulated plastic strain) shown in Figure 10 corresponding to $\alpha=35.0^{\circ}$ is quite close to that predicted by the bifurcation analysis around the time of yielding as the deformation band propagates.

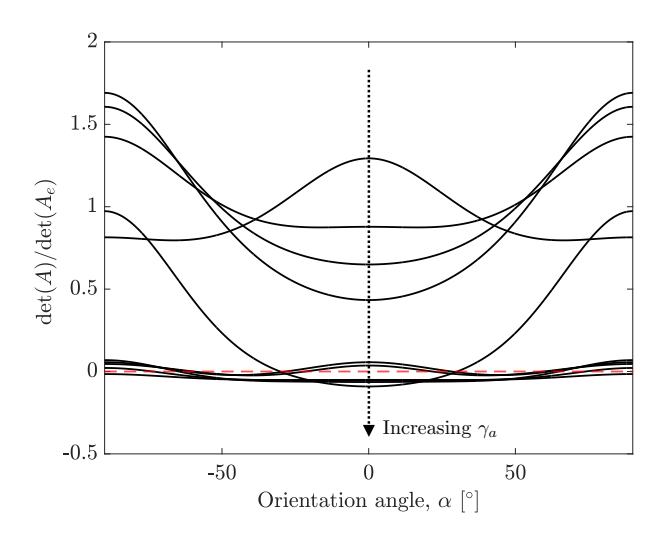


Fig. 11. Normalized acoustic tensor $\det(A)/\det(A_e)$ plotted against the band angle α with respect to the horizontal, over varying axial strain γ_a for the $\sigma_c = -2.5$ MPa simulation. The shown range of γ_a spans from 0.85 to 1.1%. Dashed red line corresponds to $\det(A)/\det(A_e) = 0$.

In Figure 12 results from the biaxial test under $\sigma_c = -4.0$ MPa are shown, including the deviatoric stress q plotted as a function of the axial strain γ_a on the left, and contours of the damage variable d on the right panels. The stress-strain curve depicts a brief elastic region followed by the initiation of two distinct horizontal

compaction bands starting at $\gamma_a=0.95\%$. The compaction bands form within the sample and do not originate from the boundaries, indicating that the SPH method can capture localization without boundary effects and without the need to introduce heterogeneities or zones of material weakness. This fact is likely the result of minuscule fluctuations in the density field which are often found in the SPH method [24]. We observe that our simulations are also able to model the spontaneous unloading in the stress-strain curve in the $\sigma_c=-4.0$ MPa laboratory test resulting from the formation of the initial localized compaction bands, although they do not occur at the exact same amounts of axial strain. After the compaction bands propagate across the entire width of the sample, softening in the stress-strain response ensues, matching the experimental laboratory test data. This softening is followed by propagation of the zones of compaction towards the sample top and bottom edges as axial deformation increases coupled with hardening in the stress-strain response, a feature observed in other numerical modeling efforts [29, 59, 93] and in experimental studies [10]. The initiation of hardening indicates that compaction and grain crushing have ended, and the crushed grains have obtained their stable configurations. From a numerical standpoint, the uninterrupted propagation of the compaction zones may be attributed to the homogeneous nature of the sample without any material heterogeneities or weak zones that attract the deformation.

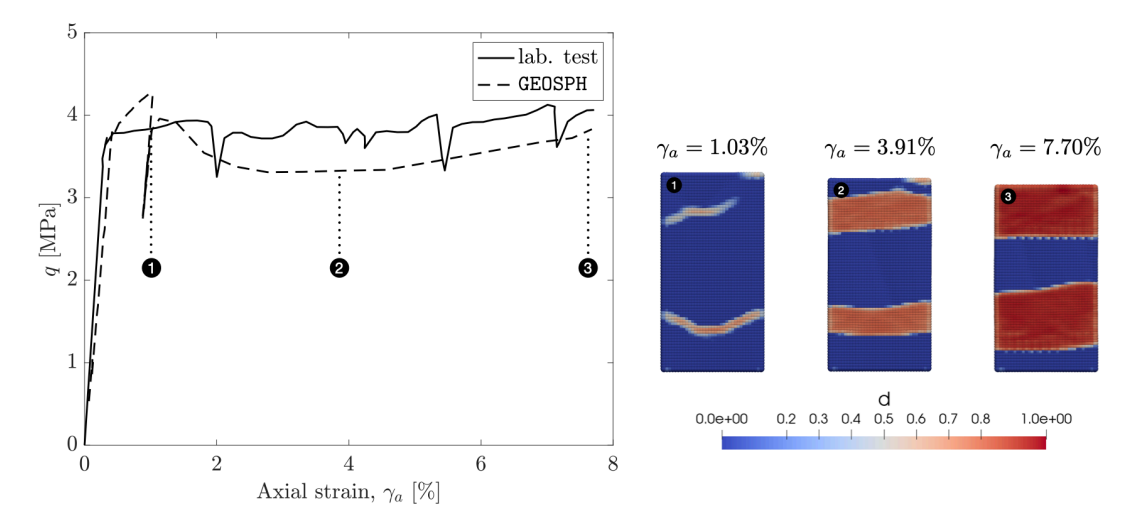


Fig. 12. Same as Figure 10, but for the $\sigma_c = -4.0$ MPa test.

A bifurcation analysis performed on the first particle (centrally located) to yield in the bottom-most deformation band in the $\sigma_c = -4.0$ MPa simulation indicates that the normalized determinant of the acoustic tensor just prior to yielding exhibits a most favorable orientation of $\alpha = \pm 35^{\circ}$, but tending to 0° (horizontal) with increasing axial strain. This pattern is mirrored in the contours of the damage variable (again matching those of the accumulated plastic strain) in Figure 12 as both deformation bands are initially inclined away from the initial yielding/damage location at around $\alpha = 25^{\circ}$ with respect to the horizontal and over time become horizontal, suggesting the formation of a pure compaction band.

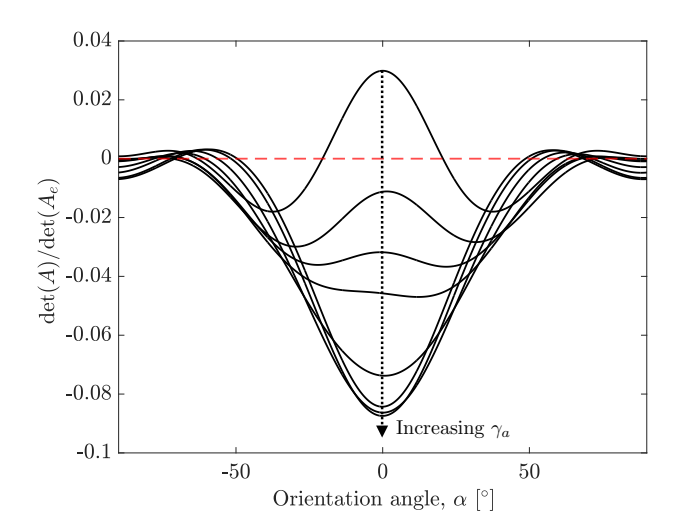


Fig. 13. Same as Figure 11 but for the $\sigma_c = -4.0$ MPa test. Note γ_a spans from 0.95 to 1%.

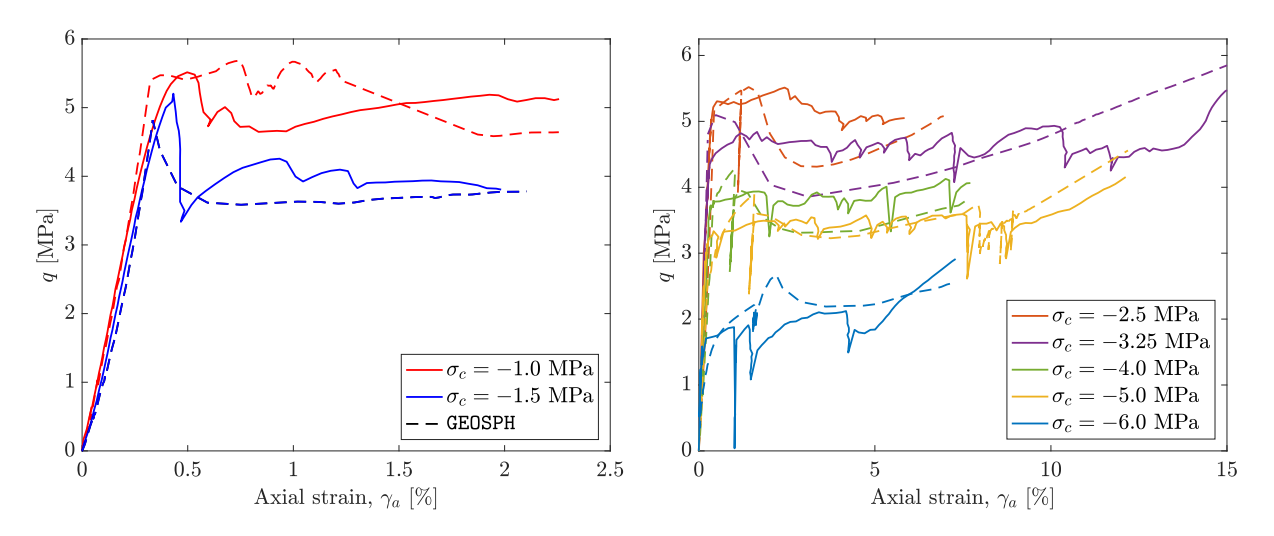


Fig. 14. Deviatoric stress q versus axial strain γ_a for the laboratory tests performed by [58] (solid lines) and the corresponding GEOSPH simulations (dashed lines) for different values of the confining pressure σ_c .

In Figure 14 the deviatoric stress versus axial strain results from all the simulations conducted by GEOSPH at different confining pressures are compared to the experimental results. The simulated stress-strain curves agree well with those from the experimental study, for both steep angled shear bands $\sigma_c = -1.0, -1.5$ MPa, for the case of a shear enhanced compaction band $\sigma_c = -2.5$ MPa, and for the horizontal compaction bands $\sigma_c = -3.25, -4.0, -5.0, -6.0$ MPa. The elastic, stress peak, softening, and hardening portions of the stress-strain curves are all present for the simulations producing compaction bands. Like in the experimental results, the stress-strain plateau that ensues after the conclusion of the compaction band propagation is shorter in duration (in terms of axial strain) for larger confining pressures. In addition, the temporal location (in terms of axial strain) of the spontaneous unloading caused by compaction band propagation is captured quite accurately for

some tests, like in the $\sigma_c = -5.0$ or -6.0 MPa simulations. In the case of low confining pressure, the SPH simulations using our elastoplastic damage model correctly predict post-peak softening after the propagation of the shear bands, and a subsequent stress-strain plateau with no significant hardening.

All the simulations presented thus far have assumed homogeneous material properties within the samples subjected to biaxial loading. Although the SPH results have shown that heterogeneity is not necessary to initiate localization and that deformation bands form in the homogeneous simulations far away from the reach of boundary effects, previous studies have demonstrated that heterogeneity increases the proclivity for strain localization 4,5,18. Also, we wish to see if heterogeneity will lead to damage and thus cause grain crushing to localize onto multiple thinner planes, rather than the wide, and freely propagating (perpendicular to their axis) zones seen in some of the notchless homogeneous Tuffeau de Maastricht simulations. To illustrate the effects of material heterogeneity on strain localization in the Tuffeau de Maastricht samples, the $\sigma_c = -2.5$ and -4.0MPa simulations are re-done under two distinct sets of random initial preconsolidation pressure $(p_c)_0$ fields. The two random $(p_c)_0$ fields are generated from a normal distribution such that its standard deviation is equal to either 1% or 3% of the mean preconsolidation pressure $(SD = 0.01(\overline{p}_c)_0)$ or $SD = 0.03(\overline{p}_c)_0)$ which is set to the value used in the previous homogeneous simulations of $(\bar{p}_c)_0 = -6.7$ MPa. This methodology ensures that the specimen will yield at various distinct locations, triggering localized grain crushing through the linkage between plasticity and damage inherent in our formulation. The two random $(p_c)_0$ fields and their corresponding normal distributions are displayed in Figure 15. Figures 16 and 17 showcase the results of the biaxial tests with $\sigma_c = -2.5$ MPa for the $SD = 0.01(\overline{p}_c)_0$ and $SD = 0.03(\overline{p}_c)_0$ fields respectively, whereas Figure 18 and 19 do so for the $\sigma_c = -4.0$ MPa simulation.

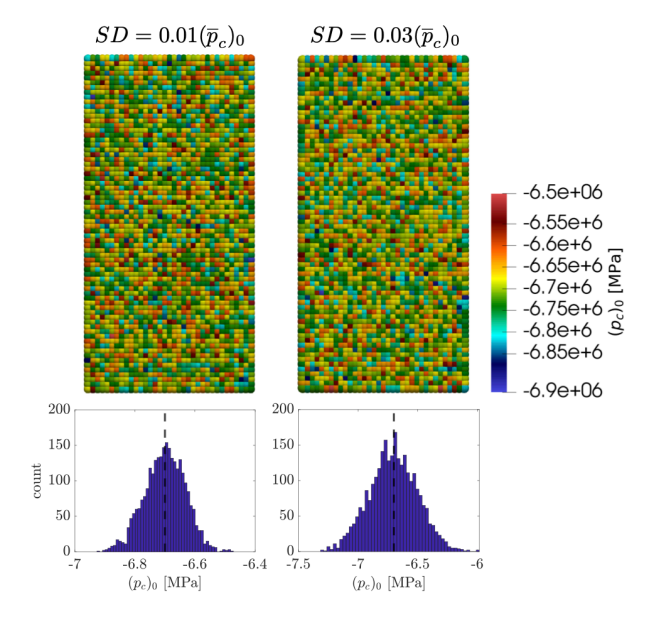


Fig. 15. Random initial preconsolidation pressure $(p_c)_0$ fields used in the heterogeneous $\sigma_c = -2.5$ and -4.0 MPa simulations. The black dashed line in the normal distributions corresponds to the mean initial preconsolidation pressure $(\bar{p}_c)_0 = -6.7$ MPa.

A salient consequence of heterogeneity in the preconsolidation pressure is the generation of secondary, low-magnitude strain localization events which precede the propagation of persistent deformation bands, and which occur prior to the peak deviatoric stress. The persistent deformation bands are of greater plastic strain magnitude than the precursory strain localization events and are accompanied by damage (grain crushing), closely resembling the deformation bands forming in the homogeneous simulations. In the biaxial test under -2.5 MPa of confining stress, the precursory localization takes orientations within $\pm 10^{\circ}$ of the ultimate persistent shear-

enhanced compaction bands, whereas for the biaxial test under a confining stress of -4.0 MPa the precursory events are considerably more disordered, although a few distinctive can be resolved to have an orientation close to 20° to 30° from the horizontal, differing significantly from the ultimate near-horizontal orientation taken by the persistent compaction bands. These observations are true for both the simulations with $SD = 0.01(\overline{p}_c)_0$ and $SD = 0.03(\bar{p}_c)_0$ random fields. In all simulation cases, the persistent deformation bands propagate perpendicular to their axis after complete propagation across the specimen just like in the homogeneous simulations, engulfing the precursory localization as grain crushing ensues. We also note that the heterogeneous nature of the sample properties does not change the general structural response of the specimen (stress-strain behavior). However, it does slightly modify the location and number of the persistent deformation bands, as well as the temporal spacing of localization events. For example, in the $SD = 0.01(\bar{p}_c)_0$, $\sigma_c = -2.5$ MPa simulation (Figure 16), the top-most band is mirrored across the y-axis of the sample, as is the bottom-most, with the bottom-most achieving the greatest ultimate thickness. While, at an axial strain of 1.28%, a band at the top seemed to grow from some of the precursory localization events, its growth is impeded once the persistent deformation band propagates. In the $SD = 0.03(\overline{p}_c)_0$, $\sigma_c = -4.0$ MPa simulation (Figure 19), only one localized zone of grain crushing emerges, rather than two like in the homogeneous simulation, here located at the top of the specimen. Evidently, throughout all the heterogeneous simulations, the random distribution of material strength leads to the formation of a variable number of preferential zones for strain localization which later amalgamate into the persistent compaction bands, changing the otherwise deterministic nature of the homogeneous simulations.

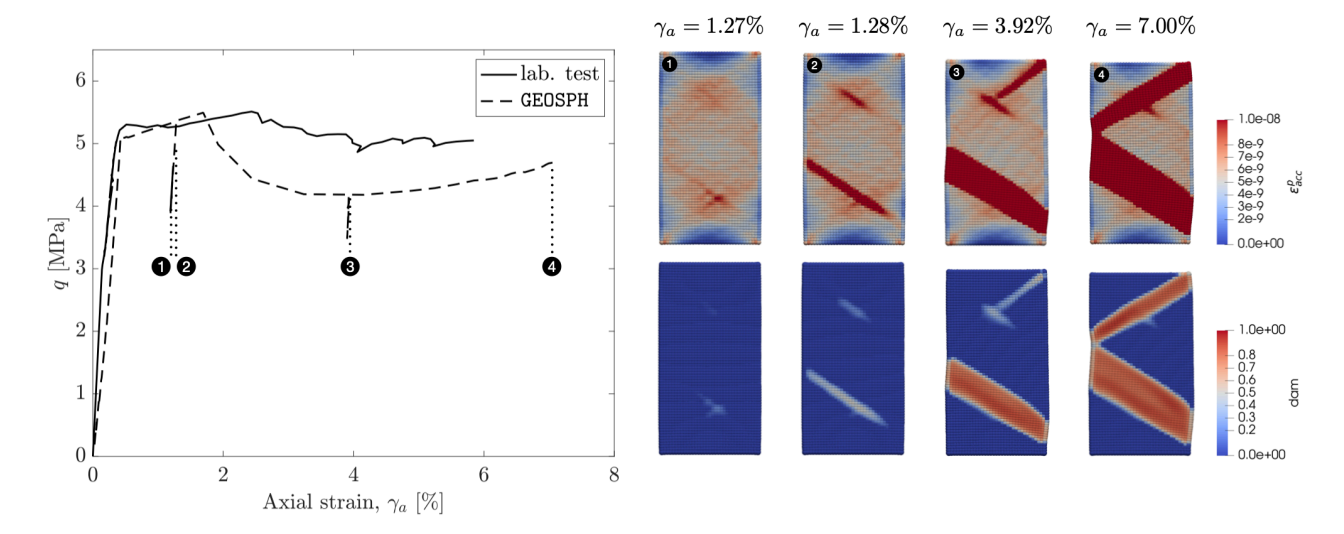


Fig. 16. (left) deviatoric stress q as a function of axial strain γ_a for the simulation performed by GEOSPH with a heterogeneous preconsolidation pressure field given $SD=0.01(\bar{p}_c)_0$ under a confining pressure of $\sigma_c=-2.5$ MPa and from the laboratory test performed by [58] given $\sigma_c=-2.5$ MPa. (right) contours of the accumulated plastic strain ε_{acc}^p at various amounts of axial strain (γ_a) for the biaxial simulation. Numbers circled in black indicate the amount of axial strain on the stress-strain plot at which the snapshots on the right-hand side are displayed.

In addition, in Figures 16 and 17 the temporal spacing (by amount of axial strain) between the two main persistent deformation bands increases substantially with respect to the original homogeneous simulation seen in Figure 10 for the tests with $\sigma_c = -2.5$ MPa. The increased spacing between the events leads to more than one spontaneous unloading event after the deformation band is fully propagated which also differs from the homogeneous results, but matches the experimental data more closely. Nevertheless, heterogeneity is not a requirement to produce more than one spontaneous unloading of the sample at the structural level as evidenced by the stress-strain curves of the homogeneous simulations with confining stress of -5.0 and -1.0 MPa in Figure 14 as the natural ability of the SPH method to trigger multiple localization events without predetermined heterogeneities or weaknesses, and instead based on small fluctuations in the density field, is sufficient. At the

same time, heterogeneity given its random nature as introduced in the samples, may not necessarily be sufficient to trigger temporally spaced spontaneous unloadings as seen in Figures 18 and 19 for the simulations with $\sigma_c = -4.0$ MPa. Overall, heterogeneity simply helps facilitate temporally distinct deformation band propagation with no definite guarantees.

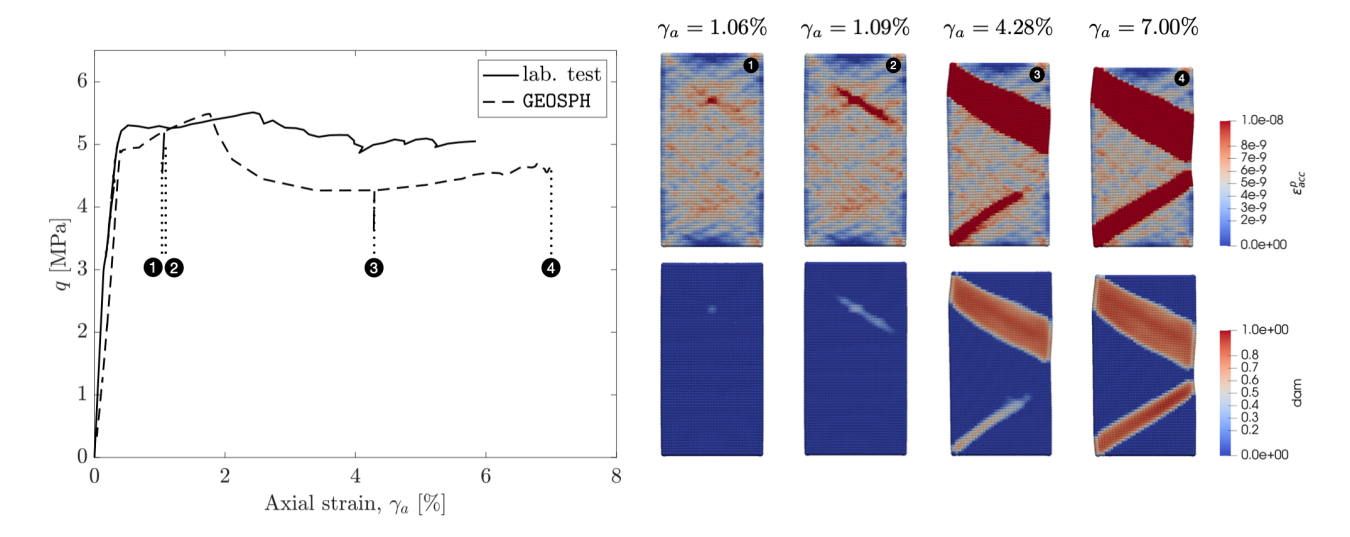


Fig. 17. (left) deviatoric stress q as a function of axial strain γ_a for the simulation performed by GEOSPH with a heterogeneous preconsolidation pressure field given $SD=0.03(\overline{p}_c)_0$ under a confining pressure of $\sigma_c=-2.5$ MPa and from the laboratory test performed by [58] given $\sigma_c=-2.5$ MPa. (right) contours of the accumulated plastic strain ε_{acc}^p at various amounts of axial strain (γ_a) for the biaxial simulation.

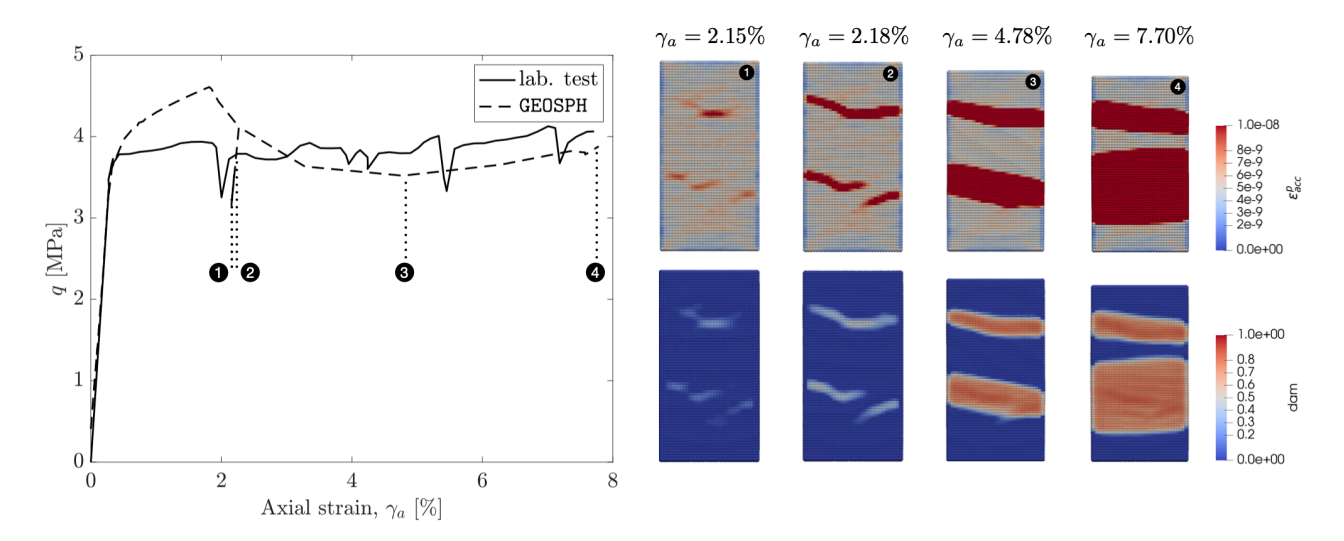


Fig. 18. Same as Figure 16 but for the simulation subject to a confining pressure of $\sigma_c = -4.0$ MPa.

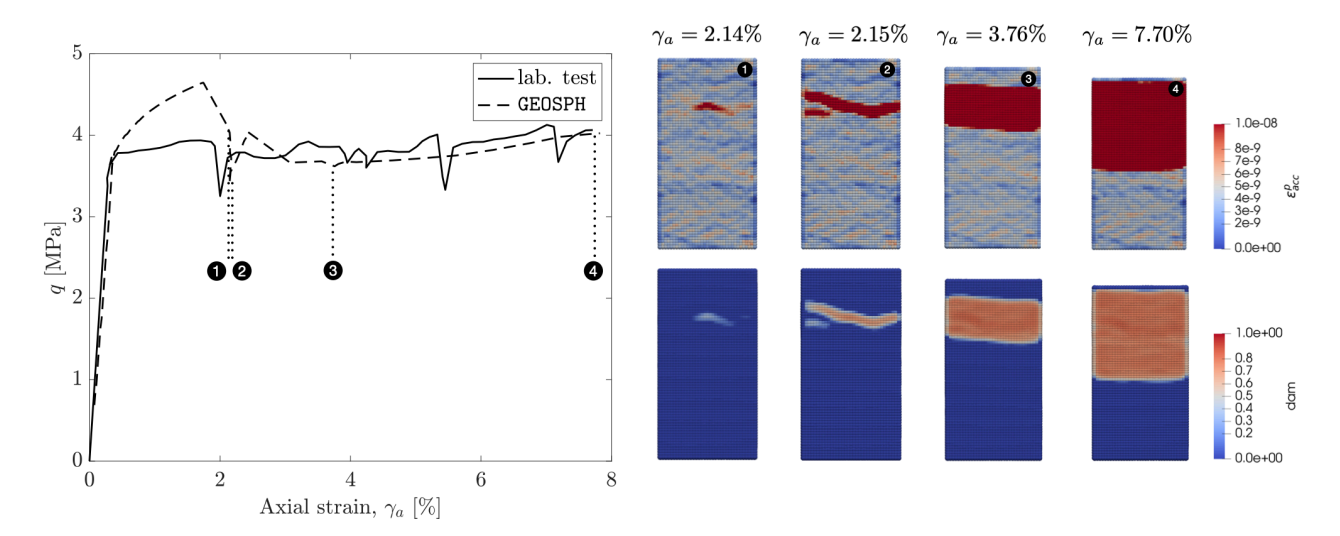


Fig. 19. Same as Figure 17 but for the simulation subject to a confining pressure of $\sigma_c = -4.0$ MPa.

The precursory localization events modeled in our simulations strongly resemble so-called microbands [63], [97] alternatively called pre-peak localization 39 or microshear bands 3 detected throughout analogue experiments and discrete simulations of granular media prior to peak stress, subsequent softening, and the development of major persistent localization 87. Pre-peak localization of deformation may coalesce giving rise to the permanent deformation band itself or be intermittent and dissipate in the wake of the permanent band forming independently 28 37. In experimental studies, these pre-peak localization events may form without satisfying the bifurcation criterion (Eq. [43]), and thus may emerge at different orientations from the persistent deformation bands 28. However, while our continuum damage model within the SPH method allows us to capture the transition from a pre-peak or precursory localization event to a persistent deformation band with localized grain crushing (and a nonzero damage variable), which mirrors experimental observations, the orientations of the precursory localization zones can actually be explained with the bifurcation criterion and the analysis shown in Figures 11 and 13 indicating that these are not two disparate events. This fact is evident in the $\sigma_c = -2.5$ MPa simulations where the persistent bands are oriented similarly to the precursory zones, and in the $\sigma_c = -4.0 \text{ MPa}$ simulations, where the precursor events take orientations matching the minima of the normalized determinant of the acoustic tensor prior to yielding around 25° to 30°, with the persistent deformation bands initially taking these orientations, and over progressive localization flattening the overall band angle towards the horizontal to form compaction bands, just as the orientation of the acoustic tensor determinant minimum trends to $\alpha = 0^{\circ}$.

5 Conclusion

In this study, we propose a kernel-based continuum damage model using the meshfree smoothed particle hydrodynamics (SPH) method designed to capture the phenomenon of compaction band formation in porous sedimentary rock. A plasticity model based on the classical modified Cam Clay model combined with an evolution equation designed to capture unstable pore collapse following grain crushing helps to successfully reproduce the softening response induced by grain crushing as well as post-crushing strain hardening seen in laboratory experiments. Two distinct SPH-based discretizations involving a nonlocal integral form and a nonlocal gradient enhanced form of the equivalent strain are developed and compared: we additionally derive the ideal relation in terms of the smoothing length that ensures the gradient approach is a second-order approximation of the integral nonlocal damage. The constitutive nonlocal properties stemming from the nonlocal damage model and the nonlocality of the SPH method itself are leveraged to ensure discretization-independent solutions. Our framework captures a number of phenomena observed in both the field and in laboratory testing. These include the

development of both pure and shear-enhanced compaction bands, including characteristic hinged-chevron type bands, a dependence of the degree of localization on the grading index, and the transition from high-angled bands to horizontal bands over increasing confining pressure in unnotched samples. Our numerical examples closely recreate the stress-strain behavior in laboratory experiments of two different types of porous sandstone, Bentheim and Berea sandstone, as well as in Tuffeau de Maastricht, a high-porosity calcarenite, and demonstrate a similar deformation band propagation process to that shown in the laboratory experiments. We also use the discontinuous bifurcation criterion to interpret the evolution of deformation band orientation in our simulations and lastly, we perform numerical experiments using random heterogeneous preconsolidation pressure fields, allowing compaction bands to emerge onto randomly determined planes of weakness rather than deterministically. Material heterogeneity also allows for the development of precursory strain localization events which precede and may develop into persistent deformation or compaction bands involving localized grain crushing and damage, highlighting yet another virtue of the proposed model.

Work is underway to extend the current model to simulate compaction bands under undrained conditions using the recently developed framework for modeling undrained loading and pore pressure buildup in the SPH method [38]. As seen in our simulations of Tuffeau de Maastricht involving unnotched geometries, in both homogeneous and heterogeneous samples, the compaction bands continue propagating or growing perpendicular to their axes, in what is likely spurious damage diffusion or growth documented in the literature for nonlocal damage models [81], [94]. While the spurious growth occurs temporally late in our simulations and does not affect the vast majority of the course of the simulations, future work can explore procedures to alleviate the damage model from this undesired response, such as lifting the assumption of a constant interaction domain, and instead varying the length scales with the principal stress state or with the degree of damage itself [84]. In addition, future research can extend the model to account for fully coupled hydromechanical processes involving permeability reduction and fluid flow across the compaction bands [53]. Other potential avenues of exploration include enhancing the current model to include the effects of material anisotropy [55], [111], [113], inertial effects [102], or creep [20], [64], [110].

Acknowledgements

This material is based upon work supported by the National Science Foundation under Award Number CMMI-1914780. The first author acknowledges the support by the U.S. National Science Foundation (NSF) Graduate Research Fellowship under Grant DGE 1656518, as well as by the Stanford Graduate Fellowship.

References

- [1] Abrari Vajari S, Neuner M, Arunachala PK, Ziccarelli A, Deierlein G, Linder C (2022). A thermodynamically consistent finite strain phase field approach to ductile fracture considering multi-axial stress states. Computer Methods in Applied Mechanics and Engineering 400:115467.
- [2] Abrari Vajari S, Neuner M, Arunachala PK, Linder C (2023). Investigation of driving forces in a phase field approach to mixed mode fracture of concrete. Computer Methods in Applied Mechanics and Engineering 417(A): 116404. Goodman AL, Frailey S, Werth CJ (2019). A review of geochemical-mechanical impacts in geological carbon storage reservoirs. Greenhouse Gases: Science and Technology 9(3):474–504.
- [3] Amirrahmat S, Druckrey AM, Alshibli KA, Al-Raoush R (2019). Micro Shear Bands: Precursor for Strain Localization in Sheared Granular Materials. Journal of Geotechnical and Geoenvironmental Engineering 145(2):04018104.
- [4] Andrade JE, Borja RI (2006). Capturing strain localization in dense sands with random density. International Journal for Numerical Methods in Engineering 67(11):1531–1564.
- [5] Andrade JE, Baker JW, Ellison KC (2008). Random porosity fields and their influence on the stability of granular media. International Journal for Numerical and Analytical Methods in Geomechanics 32:1147– 1172

- [6] Arunachala PK, Abrari Vajari S, Neuner M, Linder C (2023). A multiscale phase field fracture approach based on the non-affine microsphere model for rubber-like materials. Computer Methods in Applied Mechanics and Engineering 410: 115982.
- [7] Aydin A, Borja RI, Eichhubl P (2006). Geological and mathematical framework for failure modes in granular rock. Journal of Structural Geology 28(1): 83–98.
- [8] Barraclough TW, Blackford JR, Liebenstein S, Sandfeld S, Stratford TJ, Weinländer G, Zaiser M (2017). Propagating compaction bands in confined compression of snow. Nature Physics 13: 272–275.
- [9] Bastawros AF, Bart-Smith H, Evans AG (2000). Experimental analysis of deformation mechanisms in a closed-cell aluminum alloy foam. Journal of the Mechanics and Physics of Solids 48(2):301–322.
- [10] Baud P, Klein E, Wong T, Zhu W (2004) Compaction localization in porous sandstones: spatial evolution of damage and acoustic emission activity. Journal of Structural Geology 26:603–624.
- [11] Bažant ZP, Jirásek M (2002) Nonlocal Integral Formulations of Plasticity and Damage: Survey of Progress. Journal of Engineering Mechanics 128(11): 1119–1149.
- [12] Borja RI (2000). A finite element model for strain localization analysis of strongly discontinuous fields based on standard Galerkin approximation. Computer Methods in Applied Mechanics and Engineering 190:1529–1549.
- [13] Borja Ri, Regueiro RA (2001). Strain localization in frictional materials exhibiting displacement jumps. Computer Methods in Applied Mechanics and Engineering 190:2555–2580.
- [14] Borja RI (2004). Cam-Clay plasticity. Part V: A mathematical framework for three-phase deformation and strain localization analyses of partially saturated porous media. Computer Methods in Applied Mechanics and Engineering 193(48-51): 5301-5338.
- [15] Borja RI, Aydin A (2004). Computational modeling of deformation bands in granular media. I. Geological and mathematical framework. Computer Methods in Applied Mechanics and Engineering 193(27-29):2667– 2698.
- [16] Borja RI (2004). Computational modeling of deformation bands in granular media. II. Numerical simulations. Computer Methods in Applied Mechanics and Engineering 193 (27–29):2699–2718.
- [17] Borja RI (2002). Bifurcation of elastoplastic solids to shear band mode at finite strain. Computer Methods in Applied Mechanics and Engineering 191(46): 5287-5314.
- [18] Borja RI, Song X, Rechenmacher AL, Abedi S, Wu W (2013). Shear band in sand with spatially varying density. Journal of the Mechanics and Physics of Solids 61:219–234.
- [19] Borja RI, Chen W, Odufisan RA (2023). A constitutive framework for rocks undergoing solid dissolution. Journal of the Mechanics and Physics of Solids 173:105198.
- [20] Borja RI, Yin Q, Zhao Y (2020). Cam-Clay plasticity. Part IX: On the anisotropy, heterogeneity, and viscoplasticity of shale. Computer Methods in Applied Mechanics and Engineering 360:112695.
- [21] Borja RI (2013). Plasticity Modeling and Computation, Springer-Verlag, Berlin-Heidelberg.
- [22] Borja RI, Lee SR (1990). Cam-Clay plasticity, Part I: Implicit integration of elasto-plastic constitutive relations. Computer Methods in Applied Mechanics and Engineering 78(1), pp. 49-72.
- [23] Bui HH, Fukagawa R, Sako K, Ohno S (2008). Lagrangian meshfree particles method (SPH) for large deformation and failure flows of geomaterial using elastic-plastic soil constitutive model. International Journal for Numerical and Analytical Methods in Geomechanics 32:1537–1570.
- [24] Bui HH, Nguyen GD (2021). Smoothed particle hydrodynamics (SPH) and its applications in geomechanics: From solid fracture to granular behavior and multiphase flows in porous media. Computers and Geotechnics 138: 104315.
- [25] Buscarnera G, Laverack RT (2014). Path dependence of the potential for compaction banding: theoretical predictions based on a plasticity model for porous rocks. Journal of Geophysical Research: Solid Earth 119:1882–1903.
- [26] Chen W, Zhao Y, Borja RI (2023). Solid-fluid interaction in porous materials with internal erosion. Acta Geotechnica 18: 5147–5164.
- [27] Chen Y, Mobasher ME, Gu C, Zheng D, Waisman H (2022). Thermodynamically consistent non-local damage formulation for fluid-driven fracture in poro-viscoelastic media. Acta Geotechnica 17: 5321–5350.
- [28] Darve F, Nicot F, Wautier A, Liu J (2021). Slip lines versus shear bands: Two competing localization modes. Mechanics Research Communications 114:103603.

- [29] Das A, Buscarnera G (2014). Simulation of localized compaction in high-porosity calcarenite subjected to boundary constraints. International Journal of Rock Mechanics & Mining Sciences 71:91-104.
- [30] Das A, Nguyen GD, Einav I (2011). Compaction bands due to grain crushing in porous rocks: A theoretical approach based on breakage mechanics. Journal of Geophysical Research 116: B08203.
- [31] Das A, Nguyen GD, Einav I (2013). The propagation of compaction bands in porous rocks based on breakage mechanics. Journal of Geophysical Research 118: 2049–2066.
- [32] de Brost R, Verhoosel CV (2016). Gradient damage vs phase-field approaches for fracture: Similarities and differences. Computer Methods in Applied Mechanics and Engineering (312):78–94.
- [33] De Vree JHP, Brekelmans WAM, van Gils, MAJ (1995). Comparison of nonlocal approaches in continuum damage mechanics. Computers & Structures 55(4):581–588.
- [34] del Castillo EM, Fávero Neto AH, Borja RI (2021) Fault propagation and surface rupture in geologic materials with a meshfree continuum method. Acta Geotechnica 16:2463–2486.
- [35] del Castillo EM, Fávero Neto AH, Borja RI (2021) A continuum meshfree method for sandbox-style numerical modeling of accretionary and doubly vergent wedges. Journal of Structural Geology 153:104466.
- [36] del Castillo EM, Fávero Neto AH, Borja RI (2023). Modeling Fault Rupture Through Layered Geomaterials with SPH. In: Dyskin A, Pasternak E., eds. Multiscale Processes of Instability, Deformation and Fracturing in Geomaterials, Springer Series in Geomechanics and Geoengineering. IWBDG 2022. Springer, Cham
- [37] del Castillo EM, Ferdowsi B, Rubin AM, Schoene B (2023). Strain localization patterns and thrust propagation in 3-D discrete element method (DEM) models of accretionary wedges. Tectonics 42(8): e2022TC007707.
- [38] del Castillo EM, Fávero Neto AH, Geng J, Borja RI (2024). An SPH framework for drained and undrained loading over large deformations. International Journal for Analytical and Numerical Methods in Geomechanics https://doi.org/10.1002/nag.3790
- [39] Desrues J, Andò E, Bósuelle P, Viggiani G, Debove L, Charrier P, Toni JB (2017). Localisation Precursors in Geomaterials?. In: Papamichos E, Papanastasiou P, Pasternak E, Dyskin A., eds. *Bifurcation and Degradation of Geomaterials with Engineering Applications*, Springer Series in Geomechanics and Geoengineering. IWBDG 2017. Springer, Cham.
- [40] Duan K, Kwok CY, Ma X (2017). DEM simulations of sandstone under true triaxial compressive tests. Acta Geotechnica 12(3):495–510.
- [41] Eichhubl P, Hooker JN, Laubach SE. (2010) Pure and shear-enhanced compaction bands in Aztec Sandstone. Journal of Structutal Geology 32(12):1873–1886.
- [42] Einav I (2007). Breakage mechanics—Part I: Theory. Journal of the Mechanics and Physics of Solids 55(6):1274–1297.
- [43] Faheti R, Manzari M (2011). Error estimation in smoothed particle hydrodynamics and a new scheme for second derivatives. Computers & Mathematics with Applications 61(2): 482-498.
- [44] Fávero Neto AH, Askarinejad A, Springman SM, Borja RI (2020). Simulation of debris flow on an instrumented test slope using an updated Lagrangian continuum particle method. Acta Geotechnica 15:2757–2777.
- [45] Fávero Neto AH, Borja RI (2018). Continuum hydrodynamics of dry granular flows employing multiplicative elastoplasticity. Acta Geotechnica 13:1027–1040.
- [46] Fazio M, Chandler MR, Sauter M (2023). Permeability evolution of Bentheim Sandstone at simulated georeservoir conditions. Scientific Reports 13: 16171.
- [47] Fei F, Mia Shumon M, Elbanna AE, Choo J (2023). Phase-field model for quasi-dynamic nucleation, growth, and propagation of rate-and-state faults. International Journal for Numerical and Analytical Methods in Geomechanics 47(2):187–211.
- [48] Fossen H, Schultz RA, Torabi A (2011). Conditions and implications for compaction band formation in the Navajo Sandstone, Utah. Journal of Structural Geology 33(10):1477–1490.
- [49] Gray J, Monaghan J, Swift R (2001). SPH elastic dynamics. Computer Methods in Applied Mechanics and Engineering 190(49-50): 6641-6662.
- [50] Holcomb D, Rudnicki JW, Issen KA, Sternlof K (2007). Compaction localization in the earth and the laboratory: State of the research and research directions. Acta Geotechnica 2(1):1–5.

- [51] Hong Y, Zhang J, Zhao Y, Wang L, Wang, L (2023). Coupled hydro-mechanical XFEM analysis for multi-fracturing through an excavation driven by an underlying aquifer: a forensic case study. Acta Geotechnica.
- [52] Ip SCY, Borja RI (2022). A phase-field approach for compaction band formation due to grain crushing. International Journal for Numerical and Analytical Methods in Geomechanics 46(16):2965–2987.
- [53] Ip SCY, Borja RI (2023). Modeling heterogeneity and permeability evolution in a compaction band using a phase-field approach. Journal of the Mechanics and Physics of Solids 181:105441.
- [54] Issen KA, Rudnicki JW (2000). Conditions for compaction bands in porous rock. Journal of Geophysical Research: Solid Earth. 105(B9):21529-21536.
- [55] Jin W, Arson C (2018). Anisotropic nonlocal damage model for materials with intrinsic transverse isotropy. International Journal of Solids and Structures 139–140:29–42.
- [56] Kachanov L (1986). Introduction to continuum damage mechanics. Vol. 10. Springer Science & Business Media.
- [57] Kuhl E, Ramm E, de Borst R (2000) An anisotropic gradient damage model for quasi-brittle materials. Computer Methods in Applied Mechanics and Engineering 183:87–103.
- [58] Leuthold J, Gerolymatou G, Vergara MR, Triantafyllidis T (2021). Effect of Compaction Banding on the Hydraulic Properties of Porous Rock: Part I—Experimental Investigation. Rock Mechanics and Rock Engineering 54:2671–2683.
- [59] Leuthold J, Gerolymatou G, Vergara MR, Triantafyllidis T (2021). Efect of Compaction Banding on the Hydraulic Properties of PorousRock - Part II: Constitutive Description and Numerical Simulations. Rock Mechanics and Rock Engineering 54:2685–2696.
- [60] Linder C, Zhang X (2013). A marching cubes based failure surface propagation concept for threedimensional finite elements with non-planar embedded strong discontinuities of higher-order kinematics. International Journal for Numerical Methods in Engineering 96(6):339–372.
- [61] Liu C, Pollard DD, Deng S, Aydin A (2015). Mechanism of formation of wiggly compaction bands in porous sandstone: 1. Observations and conceptual model. Journal of Geophysical Research: Solid Earth 120(12):8138–8152.
- [62] Liu C, Pollard DD, Gu K, Shi B (2015). Mechanism of formation of wiggly compaction bands in porous sandstone: 2. Numerical simulation using discrete element method. Journal of Geophysical Research: Solid Earth 120(12):8153–8168.
- [63] Liu J, Wautier A, Zhou W, Nicot F, Darve F (2022). Incremental shear strain chain: a mesoscale concept for slip lines in 2D granular materials. Granular Matter 24(119).
- [64] Liu Y, Borja RI (2022). Time scales in the primary and secondary compression of soils. International Journal for Numerical and Analytical Methods in Geomechanics 46(8): 1383–1408.
- [65] Liu G, Liu M (2003). Smoothed Particle Hydrodynamics: A Meshfree Particle Method. World Scientific Co.
- [66] Marketos G, Bolton MD (2009). Compaction bands simulated in discrete element models. Journal of Structural Geology 31(5):479–490.
- [67] Mazars J, Pijaudier-Cabot G (1989). Continuum damage theory—Application to concrete. Journal of Engineering Mechanics 115:345–365
- [68] Menéndez B, Zhu W, Wong TF (1996). Micromechanics of brittle faulting and cataclastic flow in Berea sandstone. Journal of Structural Geology 18(1):1–16.
- [69] Mollema PN, Antonellini MA (1996). Compaction bands: a structural analog for anti-mode I cracks in aeolian sandstone. Tectonophysics 267(1–4):209–228.
- [70] Morikawa DS, Asai M (2022). Soil-water strong coupled ISPH based on u-w-p formulation for large deformation problems. Computers and Geotechnics 142: 104570.
- [71] Morikawa DS, Asai M (2022). A phase-change approach to landslide simulations: Coupling finite strain elastoplastic TLSPH with non-Newtonian IISPH. Computers and Geotechnics 148: 104815.
- [72] Morikawa DS, Asai M (2021). Coupling total Lagrangian SPH-EISPH for fluid-structure interaction with large deformed hyperelastic solid bodies. Computer Methods in Applied Mechanics and Engineering 381: 113832
- [73] Morris JP, Fox PJ, Zhu Y (1997) Modeling low Reynolds number incompressible flows using SPH. Journal of Computational Physics 136(1): 214–226

- [74] Mukhtar FM, Shauer N, Duarte CA (2022). Propagation mechanisms and parametric influence in multiple interacting hydraulic fractures: A 3-D G/XFEM hydro-mechanical modeling. International Journal for Numerical and Analytical Methods in Geomechanics 46(11):2033–2059.
- [75] Mullet B, Segall P, Neto AF (2023). Numerical modeling of caldera formation using Smoothed Particle Hydrodynamics (SPH). Geophysical Journal International 234(2): 887–902.
- [76] Neuner M, Abrari Vajari S., Arunachala PK, Linder C (2022). A better understanding of the mechanics of borehole breakout utilizing a finite strain gradient enhanced micropolar continuum model. Computers and Geotechnics 153:105064.
- [77] Olsson WA, Holcomb DJ, Rudnicki JW (2002). Compaction localization in porous sandstone: Implications for reservoir mechanics. Oil & Gas Science and Technology 57(5):591–599.
- [78] Papka SD, Kyriakides S (1998). Experiments and full-scale numerical simulations of in-plane crushing of a honeycomb. Acta Materialia 46(8):2765-2776.
- [79] Peerlings RHJ, de Borst R, Brekelmans, WAM, Geers MGD (1998). gradient enhanced damage modelling of concrete fracture. Mechanics of Cohesive-Frictional Materials 3:323–342.
- [80] Peerlings RHJ, de Borst R, Brekelmans WAM, De Vree JHP (1996). Gradient enhanced damage for quasi-brittle materials. International Journal for Numerical Methods in Engineering 39(19):3391–3403.
- [81] Pereira LF, Weerheijm J, Sluys LJ (2016). A new rate-dependent stress-based nonlocal damage model to simulate dynamic tensile failure of quasi-brittle materials. International Journal of Impact Engineering 94:83–95.
- [82] Pereira GG, Cleary PW, Lemiale V (2017). SPH method applied to compression of solid materials for a variety of loading conditions. Applied Mathematical Modelling 44: 72–90
- [83] Pijaudier-Cabot G, Bažant Z (1987). Nonlocal damage theory. Journal of Engineering Mechanics 113(10):1512–1533.
- [84] Poh LH, Sun G (2017). Localizing gradient damage model with decreasing interactions. International Journal for Numerical Methods in Engineering 110(6):503–522.
- [85] Ramachandran P, Bhosale A, Puri K, et al (2021). PySPH: A Python-based framework for smoothed particle hydrodynamics. ACM Transactions on Mathematical Software (TOMS) 47(4):1–38.
- [86] Rattez H, Shi Y, Sac-Morane A, Klaeyle T, Mielniczuk B, Veveakis M (2022). Effect of grain size distribution on the shear band thickness evolution in sand. Géotechnique 72(4):350–363.
- [87] Rechemmacher AL (2006). Grain-scale processes governing shear band initiation and evolution in sands. Journal of the Mechanics and Physics of Solids 54:2–45.
- [88] Rudnicki JW, Rice K (1975). Conditions for the localization of deformation in pressure-sensitive dilatant materials. Journal of the Mechanics and Physics of Solids 23(6): 371–394.
- [89] J Rutqvist (2012). The geomechanics of CO_2 storage in deep sedimentary formations. Geotechnical and Geological Engineering. 30(3):525-551.
- [90] Ryan EM, Tartakovsky AM, Amon C (2010). A novel method for modeling Neumann and Robin boundary conditions in smoothed particle hydrodynamics. Computer Physics Communications 181(12): 2008–2023
- [91] Sanz PF, Borja RI, Pollard DD. Mechanical aspects of thrust faulting driven by far-field compression and their implications for fold geometry. Acta Geotechnica 2:7–31.
- [92] Sanz PF, Pollard DD, Allwardt PF, Borja RI (2008). Mechanical models of fracture reactivation and slip on bedding surfaces during folding of the asymmetric anticline at Sheep Mountain, Wyoming. Journal of Structural Geology 30: 1177–119.
- [93] Shahin G, Papazoglou A, Marinelli F, Buscarnera G (2019). Simulation of localized compaction in Tuffeau de Maastricht based on evidence from X-ray tomography. International Journal of Rock Mechanics and Mining Sciences 121: 104039.
- [94] Shedbale AS, Sun G, Poh LH (2021). A localizing gradient enhanced isotropic damage model with Ottosen equivalent strain for the mixed-mode fracture of concrete. International Journal of Mechanical Sciences 199:106410.
- [95] Suk Suh H, Sun W (2022). Multi-phase-field microporomechanics model for simulating ice-lens growth in frozen soil. International Journal for Numerical and Analytical Methods in Geomechanics 46(12):2307-2336.

- [96] Tembe S, Vajdova V, Wong T, Zhu W (2006). Initiation and propagation of strain localization in circumferentially notched samples of two porous sandstones 111:B02409.
- [97] Tordesillas A, Zhou S, Bailey J, Bondell H (2022). A representation learning framework for detection and characterization of dead versus strain localization zones from pre-to post-failure 24(75).
- [98] Vajdova V, Wong TF (2003). Incremental propagation of discrete compaction bands: acoustic emission and microstructural observations on circumferentially notched samples of Bentheim. Geophysical Research Letters 30:1775.
- [99] Vignjevic R, Djordjevic N, Gemkow S, De Vuyst T, Campbell J (2014). SPH as a nonlocal regularisation method: Solution for instabilities due to strain-softening. Computer Methods in Applied Mechanics and Engineering 277:281–304.
- [100] Violeau D (2012). Fluid Mechanics and the SPH Method. Oxford University Press.
- [101] Wang Y, Bui HH, Nguyen GD, Ranjith PG (2019). A new SPH-based continuum framework with an embedded fracture process zone for modelling rock fracture. International Journal of Solids and Structures 159:40–57.
- [102] Wang Y, Borja RI, Wu W (2023). Dynamic strain localization into a compaction band via a phase-field approach. Journal of the Mechanics and Physics of Solids 173:105228.
- [103] Wang Y, Javadi AA, Fidelibus C (2023). A hydro-mechanically-coupled XFEM model for the injection-induced evolution of multiple fractures. International Journal for Numerical and Analytical Methods in Geomechanics 47(9): 1539–1558.
- [104] Wendland H (1995). Piecewise polynomial, positive definite and compactly supported radial functions of minimal degree. Advances in Computational Mathematics 4(1): 389-296
- [105] Wong TF, David C, Zhu W (1997). The transition from brittle faulting to cataclastic flow in porous sandstones: mechanical deformation. Journal of Geophysical Research: Solid Earth. 102(B2):3009–3025.
- [106] Wu CY, Ruddy OM, Bentham AC, Hancock BC, Best SM, JA Elliott. Modelling the mechanical behaviour of pharmaceutical powders during compaction. Powder Technology. 152(1–3):107–117.
- [107] Xiong H, Hao M, Zhao D, Qiu Y, Chen X (2023). Study of the dynamics of water-enriched debris flow and its impact on slit-type barriers by a modified SPH–DEM coupling approach. Acta Geotechnica. https://doi.org/10.1007/s11440-023-02106-w
- [108] Xiong H, Qiu Y, Shi X, Wang X, Chen X (2024). Arching development above active trapdoor: insight from multi-scale analysis using FEM-SPH. Acta Geotechnica.
- [109] Yang E, Bui HH, Sterck HD, Nguyen G (2020). A scalable parallel computing SPH framework for predictions of geophysical granular flows. Computers and Geotechnics 121: 103474.
- [110] Yin Q, Liu Y, Borja RI (2021). Mechanisms of creep in shale from nanoscale to specimen scale. Computers and Geotechnics 136:104138.
- [111] Zhang Q, Choo J, Borja RI (2019). On the preferential flow patterns induced by transverse isotropy and non-Darcy flow in double porosity media. Computer Methods in Applied Mechanics and Engineering 353:570–592.
- [112] Zhao S, Bui HH, Lemiale V, Nguyen GD, Darve F (2019). A generic approach to modelling flexible confined boundary conditions in SPH and its application. International Journal for Numerical and Analytical Methods in Geomechanics 43(5): 1005–1031
- [113] Zhao Y, Borja RI (2022). A double-yield-surface plasticity theory for transversely isotropic rocks. Acta Geotechnica, DOI:10.1007/s11440-022-01605-6.